International Journal of Pharmaceutics 617 (2022) 121578

Contents lists available at ScienceDirect

International Journal of Pharmaceutics

journal homepage: www.elsevier.com/locate/ijpharm

Photothermal MnO_2 nanoparticles boost chemo-photothermal therapy-induced immunogenic cell death in tumor immunotherapy

Zhenzhen Chen [a,b,1], Qian Zhang [a,1], Qinbiao Huang [c], Zhihong Liu [b], Lingjun Zeng [b], Lingna Zhang [b], Xu Chen [b], Hongtao Song [a,b,*], Jialiang Zhang [a,b,*]

[a] College of Pharmacy, Fujian Medical University, Fuzhou 350108, PR China
[b] Department of Pharmacy, Fuzong Clinical Medical College of Fujian Medical University (900 Hospital of the Joint Logistics Team), Fuzhou 350025, PR China
[c] School of Pharmacy, Fujian University of Traditional Chinese Medicine, Fuzhou 350108, China

ARTICLE INFO

Keywords:
Photothermal MnO_2 nanoparticles
Chemo-photothermal therapy
Modulation of tumor microenvironment
Immunogenic cell death
Tumor immunotherapy

ABSTRACT

The induction of immunogenic cell death (ICD) is an attractive strategy for generating *in situ* autologous tumor cell-based vaccines and thus has great potential in cancer prevention and personalized immunotherapy. However, the effectiveness of ICD in tumor immunotherapy has been greatly limited, mainly by low induction efficiency and the immunosuppressive tumor microenvironment (TME). Herein, we report a new strategy for chemo-photothermal therapy-induced ICD by employing photothermal MnO_2 nanoparticles loaded with doxorubicin (DOX) in tumor immunotherapy to overcome the low efficiency of traditional ICD inducers and the immunosuppressive TME. Specifically, we prepared photothermal bovine serum albumin (BSA)-templated MnO_2 NPs (BSA/MnO_2 NPs) with good aqueous dispersibility and high biocompatibility through the direct reduction of $KMnO_4$ with BSA, and we then efficiently loaded DOX, an ICD inducer, onto the MnO_2 NPs through coordination (DOX-BSA/MnO_2 NPs). The DOX-BSA/MnO_2 NPs achieved high photothermal conversion efficiency, highly efficient tumor targeting, TME-responsive DOX release and modulation of the hypoxic TME. Notably, a marked *in vivo* synergistic therapeutic effect was achieved in a triple-negative breast carcinoma-bearing mouse model by combining chemo-photothermal therapy-induced ICD with amelioration of the immunosuppressive TME. Our research highlights the great promise of modulating the TME with photothermal MnO_2 nanosystems to enhance ICD-induced antitumor immunotherapy.

1. Introduction

The induction of immunogenic cancer cell death (ICD) can be used to obtain *in situ* autologous tumor vaccines that produce neoantigens and enhance immunogenicity rapidly and inexpensively (Duan et al., 2019). In response to ICD inducers, dying tumor cells can expose calreticulin (CRT) and secrete damage-associated molecular pattern molecules (DAMPs), such as high mobility group box-1 (HMGB-1) and adenosine triphosphate (ATP) (Heshmati Aghda et al., 2020). These DAMPs recruit dendritic cells (DCs) into the tumor tissue, trigger the uptake and processing of tumor antigens by DCs, and promote antigen presentation by DCs to T cells, and these effects ultimately lead to lasting antitumor immunity (Li et al., 2019; Zheng et al., 2021). Traditional tumor treatments; such as some chemotherapeutic agents (e.g., doxorubicin (DOX), oxaliplatin, and mitoxantrone), radiation therapy, and phototherapy, can induce ICD (Galluzzi et al., 2020). However, the effectiveness of ICD for tumor immunotherapy and thus its clinical application are limited, mainly by the low efficiency of ICD induction and the immunosuppressive tumor microenvironment (TME) (Zhang et al., 2021).

The nanodelivery of ICD inducers is one of the solutions developed for the above mentioned problems (Sun et al., 2021; Janicka and Gubernator, 2017). Among the nanodelivery systems reported, MnO_2 nanostructures have attracted substantial attention as a unique type of TME-responsive delivery vehicle for ICD inducers with many unique advantages: (1) MnO_2 nanostructures can react with either H^+ or glutathione (GSH) in the TME to generate Mn^{2+} ions that can function as potent adjuvants (Hou et al., 2020), and (2) MnO_2 nanostructures degrade H_2O_2 present in the TME into O_2 to relieve tumor hypoxia, which results in the transformation of tumor-associated macrophages (TAMs) from M2-type TAMs to M1-type TAMs and inhibition of the

* Corresponding authors at: College of Pharmacy, Fujian Medical University, Fuzhou 350108, PR China.
E-mail addresses: sohoto@vip.163.com (H. Song), zjlqingdao@126.com (J. Zhang).
[1] These authors contributed equally to this paper

https://doi.org/10.1016/j.ijpharm.2022.121578
Received 17 November 2021; Received in revised form 6 February 2022; Accepted 10 February 2022
Available online 14 February 2022

proliferation of regulatory T cells (Tregs) to reprogram the immunosuppressive TME (Ding et al., 2021; Xu et al., 2021). However, despite all benefits, the synthesis of MnO_2 nanostructures is usually complex and time consuming and requires relatively harsh conditions. To combine multiple ICD induction modalities, multiple drugs need to be coloaded on MnO_2 nanoparticles, which increases the cost and complexity of the synthesis and thus results in low reproducibility (Qian et al., 2020). Compared with conventional MnO_2 nanoparticles, protein-templated MnO_2 nanoparticles have unique advantages, such as fast and facile synthesis, green synthesis conditions, and good biocompatibility, and these particles have been thoroughly investigated as nanotheranostic agents (Pan et al., 2017; Xiao et al., 2018; Xiao et al., 2021). However, despite these discoveries, there are few known methods for the systematic development of protein-templated MnO_2 as an ICD nanoinducer with the capability of high-performance photothermal conversion and the ability to modulate the hypoxic TME to enhance antitumor immunity.

In this study, we therefore designed and prepared an intelligent platform based on bovine serum albumin (BSA)-templated MnO_2 nanoparticles using a simple, rapid and efficient method of reducing $KMnO_4$ with the amino and sulfhydryl groups of BSA. The ICD inducer DOX was then efficiently loaded onto the generated BSA/MnO_2 NPs (DOX-BSA/MnO_2 NPs) through coordination between MnO_2 and DOX. We subsequently demonstrated that the DOX-BSA/MnO_2 NPs exhibited high-performance photothermal conversion and could achieve tumor-targeted drug delivery, the TME-triggered controllable release of DOX, and the TME-responsive generation of O_2 to overcome tumor hypoxia. Importantly, we also demonstrated that chemo-photothermal therapy mediated by DOX-BSA/MnO_2 NPs resulted in effective growth inhibition of primary tumors. In addition, we found that combination therapy with this novel nanoagent could effectively regulate the immunosuppressive TME through the upregulation of M1-type TAMs and the down-regulation of Tregs, which resulted in the elicitation of robust antitumor immunity and the inhibition of distant tumor growth *via* a remarkable abscopal effect (Scheme 1).

2. Materials and methods

2.1. Materials

Bovine serum albumin (BSA) was purchased from Sigma–Aldrich. $KMnO_4$ was purchased from Sinopharm Chemical Reagent Co., Ltd. (Shanghai, China). Doxorubicin (DOX) was obtained from Shanghai Aladdin Bio-Chem Technology Co., Ltd. Indocyanine green (ICG) was purchased from Tokyo Chemical Industry Co., Ltd. (Shanghai, China). Alexa Fluor 488-CRT antibody was purchased from Beijing Biosynthesis

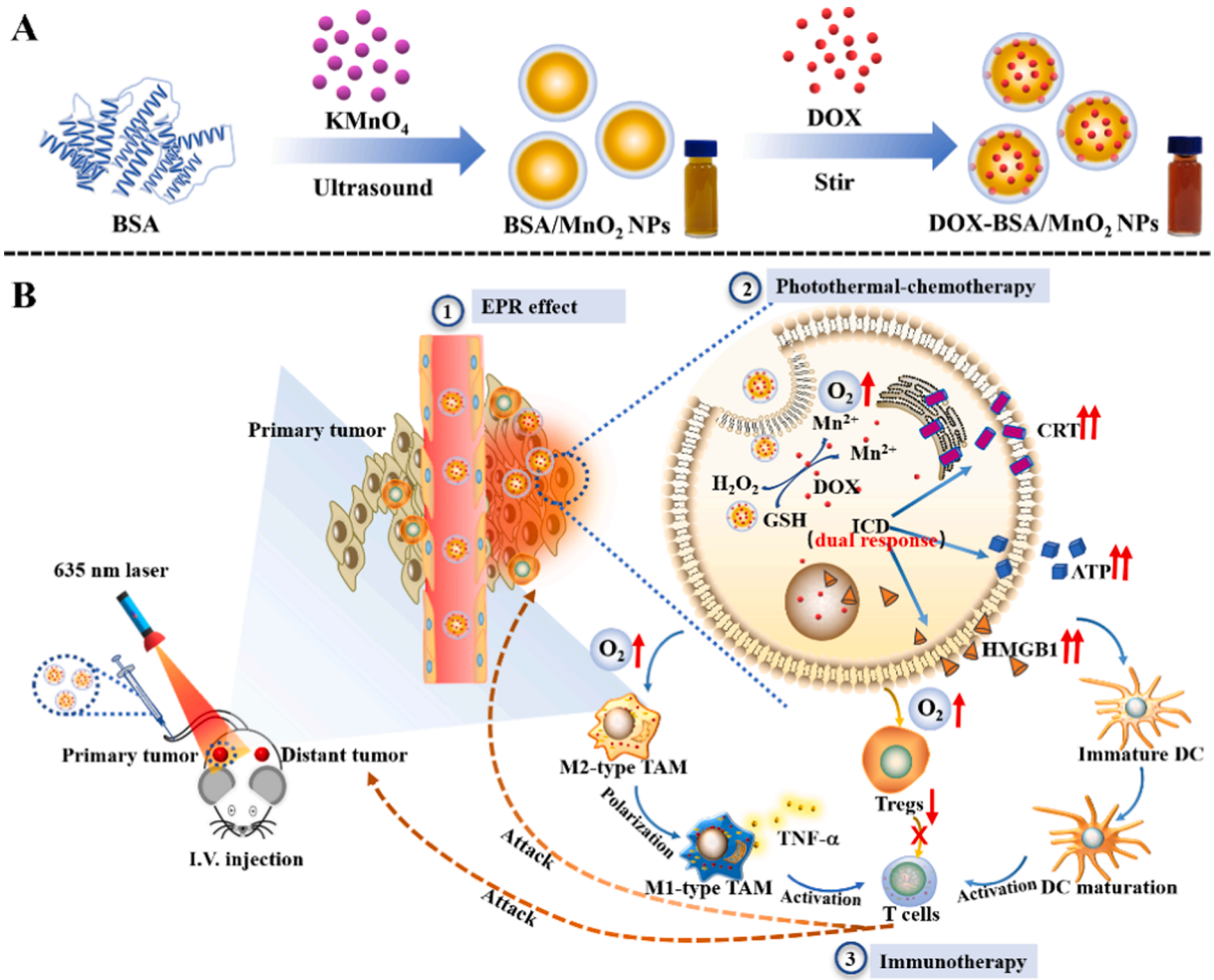

Scheme 1. Schematic illustration of (A) BSA/MnO_2 NPs synthesized through a facile *in situ* redox reaction involving the simple mixing of $KMnO_4$ and BSA solutions. To obtain the DOX-BSA/MnO_2 NPs, DOX was loaded on BSA/MnO_2 NPs through the coordination between Mn and the anthraquinone rings of DOX. (B) DOX-BSA/MnO_2 NP-mediated chemo-photothermal therapy can inhibit the growth of primary tumors and effectively shape the immunosuppressive microenvironment to favor antitumor immunity, which exerts an abscopal effect to inhibit the growth of distant tumors through the regulation of immune cell composition. (abbreviations: EPR: enhanced permeability and retention; DOX: doxorubicin; GSH: glutathione; ICD: immunogenic cell death; CRT: calreticulin; HMGB-1: high mobility group box-1; ATP: adenosine triphosphate; DC: dendritic cell; TAM: tumor-associated macrophage; Treg: regulatory T cell).

Biotechnology Co., Ltd. (Beijing, China). A mouse high mobility group protein box-1 (HMGB-1) ELISA kit was purchased from Wuhan Huamei Biological Engineering Co., Ltd. (Wuhan, China). An ATP content assay kit was obtained from Beijing Solarbio Science & Technology Co., Ltd. (Beijing, China). Fetal bovine serum (FBS) was obtained from Elite (Marburg, Germany). An Annexin V-APC/7-AAD apoptosis detection kit, Dulbecco's Modified Eagle's Medium (DMEM), Roswell Park Memorial Institute 1640 (RPMI 1640) and 3-(4,5-dimethylthiazol-2-yl)-2,5-diphenyltetrazolium bromide (MTT) were purchased from Keygen Biotech Corp., Ltd. (Jiangsu, China). All the antibodies used in the flow cytometry assay and the Cytometric Bead Array (CBA) Kit were purchased from BD Biosciences (California, USA). Water was purified using a Milli-Q system (Millipore, USA). The antibodies used for immunofluorescence analyses were purchased from Wuhan Servicebio Technology Co., Ltd. (Wuhan, China). Other chemicals of analytical grade were purchased from Sigma–Aldrich (St. Louis, MO, USA) and were used without further purification unless otherwise indicated.

2.2. Methods

2.2.1. Synthesis of DOX-BSA/MnO_2 NPs

BSA/MnO_2 NPs were synthesized through a facile one-step method using BSA as a template and reductant as described in a previous report with some modifications (Wang et al., 2019). Briefly, 20 mg of $KMnO_4$ was fully dissolved in 5 mL of deionized water, and 5 mL of BSA solution (20 mg/mL) was then added dropwise into the $KMnO_4$ solution in a water bath sonicator (100 W, KQ-800KDE, Kunshan, China). Continuous ultrasonication of the mixture for 1 h yielded the BSA/MnO_2 NPs. Subsequently, 1 mL of the obtained BSA/MnO_2 NPs was mixed with 1 mL of DOX·HCl solution (2 mg/mL) under stirring for 5 h to obtain the DOX-BSA/MnO_2 NPs. The DOX-BSA/MnO_2 NPs were purified by dialysis against deionized water for 24 h using a dialysis bag (MD44, Viskase, USA) with a 14-kDa molecular weight cutoff (MWCO). The purified DOX-BSA/MnO_2 NPs were then stored at 4 °C for further use. ICG-BSA/MnO_2 NPs were prepared using the same method as that used for the DOX-BSA/MnO_2 NPs with the exception that 1 mL of ICG solution (2 mg/mL) was used instead of DOX·HCl solution.

2.2.2. Characterization

A dynamic laser scattering instrument (Litesizer 500; Anton-Paar, Graz, Austria) was used to measure the size, polydispersity index (PDI), and zeta potential of the obtained nanoparticles. The morphology of the nanoparticles was characterized by transmission electron microscopy (TEM, JEM-2100; JOEL, Tokyo, Japan). The concentration of Mn^{4+} was determined by inductively coupled plasma–optical emission spectrometry (ICP–OES, iCAP7000, Thermo, USA). The chemical state of MnO_2 was measured by inductively coupled X-ray photoelectron spectroscopy (XPS, Xi250, Thermo, USA). The ultraviolet–visible (UV–vis) spectra of the nanoparticles were obtained by a UV–vis spectrophotometer (TU-1901, Puxi, China).

For measurement of the encapsulation efficiency (EE%) and loading efficiency (LE%), the DOX-BSA/MnO_2 NPs were ultrafiltered at 5000 rpm for 6 min with a Centriprep® 100 K centrifuge tube (MWCO = 100 kDa, EMD Millipore Corporation, Billerica, MA, USA). The filtrate was collected and analyzed by high-performance liquid chromatography (HPLC) to determine the content of free DOX·HCl (m_f). The HPLC-based quantification of doxorubicin is described in the Supplementary Methods. The filtrate was lyophilized and weighed (m_n). The EE% and LE% of DOX-BSA/MnO_2 NPs were calculated according to Eqs. (1) and (2), respectively, where m_a represents the dosing amount of DOX·HCl.

$$EE\% = \left(1 - m_f/m_a\right) \times 100\% \quad (1)$$

$$LE\% = \left(m_a - m_f\right)/m_n \times 100\% \quad (2)$$

The stability of the DOX-BSA/MnO_2 NPs was investigated by measuring the changes in their particle size and PDI in saline medium containing 10% FBS over a 7-day period at 37 °C. The stability of the DOX-BSA/MnO_2 NPs after irradiation was also investigated. Briefly, 1 mL of the DOX-BSA/MnO_2 NPs (MnO_2 dose of 100 μg/mL) in saline medium was irradiated at 1.5 W/cm^2 for 10 min (635 nm), and the variation in the particle size and PDI over a 7-day period at 37 °C was recorded.

2.2.3. In vitro photothermal performance of BSA/MnO_2 NPs

The photothermal performance of the BSA/MnO_2 NPs was evaluated by irradiating a 96-well culture plate containing aqueous dispersions of the BSA/MnO_2 NPs at different concentrations (MnO_2 doses of 0, 50, 100, 150, and 200 μg/mL) with a 635-nm semiconductor laser (Hi-Tech Optoelectronics Company, China) at a power density of 1.0 W/cm^2 for 10 min. Another experiment was performed to study the effect of power density on the photothermal performance of the BSA/MnO_2 NPs. A 96-well culture plate containing a solution of the BSA/MnO_2 NPs (MnO_2 dose of 100 μg/mL) was irradiated with a 635-nm semiconductor laser at power densities of 0.5, 1, 1.5 and 2 W/cm^2 for 10 min. Purified water was used as a control. The pre- and postirradiation temperature changes were measured and recorded using an infrared thermal imaging camera (Fotric 325, China).

To evaluate the photothermal stability, the BSA/MnO_2 NPs (MnO_2 dose of 100 μg/mL) were irradiated at 635 nm (1.5 W/ cm^2, 10 min; laser on) and then cooled to room temperature without irradiation (laser off). The laser on/off cycles were repeated four times, and the temperature was monitored.

2.2.4. In vitro release studies

The *in vitro* release experiment was conducted using the dialysis method. Briefly, 1 mL of the DOX-BSA/MnO_2 NP suspension was added to a dialysis bag (MWCO = 14 kDa), and the bag was subsequently incubated in 15 mL of PBS (10 mM, pH 7.4 or 5.5) solution containing 300 mg of BSA with stirring (100 rpm) at 37 °C. Another control experiment was performed to study the effects of H_2O_2 and GSH on the release of DOX from the DOX-BSA/MnO_2 NP suspension. The experimental method was the same as that used in the DOX release experiments with different pH conditions with the exception that H_2O_2 and GSH were added to the release solution at final concentrations of 100 μM and 5 mM, respectively. The concentrations of H_2O_2 and GSH were determined according to previous research (Zhuang et al., 2020). To investigate the influence of the photothermal effect on DOX release, the DOX-BSA/MnO_2 NPs were first irradiated for 10 min with a 635-nm laser (1.5 W/cm^2) before addition into the dialysis bag. At scheduled time points, 1 mL of release solution was collected, and an equal volume of fresh release solution was supplied. The amount of DOX in the release solution was measured by HPLC.

2.2.5. In vitro O_2 production

The O_2 generated by the DOX-BSA/MnO_2 NPs under different conditions at 37 °C was measured in a sealed chamber coupled with a portable dissolved oxygen meter (AZ-8402, Guangdong, China). Briefly, 2 mL of DOX-BSA/MnO_2 solution (MnO_2 dose of 100 μg/mL) was dispersed in 12 mL of PBS (10 mM, pH7.4 or 5.5), and the initial value of the dissolved O_2 was detected by immersing the electrode in the medium for 10 min·H_2O_2 was then injected into the chamber to a final concentration of 100 μM, and the amount of generated O_2 at predetermined time points was recorded.

2.2.6. Cell culture

The 4T1, LO2, and HEK 293T cell lines were all purchased from the Shanghai Institute for Biological Sciences Cell Resource Center. For cell culture, 4T1 and LO2 cells were incubated in RPMI 1640 with 10% FBS, 80 units/mL penicillin, and 80 μg/mL streptomycin at 37 °C under 5% CO_2. HEK 293T cells were incubated in DMEM with 10% FBS, 80 units/mL penicillin, and 80 μg/mL streptomycin at 37 °C under 5% CO_2.

2.2.7. Cytotoxicity of the BSA/MnO_2 NPs

The cytotoxicity of the BSA/MnO_2 NPs was assessed through the MTT assay. Briefly, LO2 and HEK 293T cells were seeded in 96-well plates at densities of 1×10^4 cells/well. After overnight incubation, the medium was replaced with fresh medium containing different concentrations of the BSA/MnO_2 NPs, and the cells were incubated at 37 °C for 24 h. Finally, the cell viability was measured by the MTT assay. Briefly, 20 μL of MTT reagent (5 mg/mL) was added to each well, and the plate was incubated for 4 h at 37 °C. Subsequently, 150 μL of DMSO was added to each well to completely dissolve the formazan crystals. The absorbance of each well at 570 nm was measured using a microplate reader (Model 680, Bio–Rad, USA). The results are representative of six independent experiments.

2.2.8. Cytotoxicity of the DOX-BSA/MnO_2 NPs

The cytotoxicity of DOX-BSA/MnO_2 NP-mediated chemotherapy was measured by the MTT assay. 4T1 cells were seeded in a 96-well plate at densities of 5×10^3 cells/well. After overnight incubation, the medium was replaced with fresh medium, and free DOX solution and various concentrations of the DOX-BSA/MnO_2 NPs were added. After incubation for another 24 h, the absorbance of each well at 570 nm was measured using a microplate reader. The data shown are representative of six independent experiments. The half maximal inhibitory concentration (IC50) values were calculated with GraphPad Prism 8.3.0.

The cytotoxicity of DOX-BSA/MnO_2 NP-mediated chemo-photothermal therapy was also evaluated by the MTT assay. 4T1 cells were seeded in a 96-well plate at a density of 5×10^3 cells/well and incubated overnight to allow cell attachment. The medium was then replaced with fresh medium containing different formulations of the BSA/MnO_2 NPs or DOX-BSA/MnO_2 NPs. The final concentrations of DOX and MnO_2 in all media containing these compounds were 5 μM and 100 μg/mL, respectively. The cells were then incubated at 37 °C under 5% CO_2 for another 4 h and then treated with laser irradiation at a power density of 1.5 W/cm^2 (635 nm) for 0, 1, 3, 5, 7 and 10 min. After incubation for another 20 h, the cell viability was measured by the MTT assay.

2.2.9. In vitro cell uptake

4T1 cells were seeded in laser confocal dishes (15 mm in diameter) at a density of 1×10^5 cells/well and incubated overnight to allow cell attachment. The medium was then replaced with fresh medium containing the DOX-BSA/MnO_2 NPs (5 μM DOX) for different incubation times (0.5, 2, 4, and 6 h). After three washes with PBS, the cells were fixed with 4% formaldehyde for 30 min. Subsequently, the cell nuclei were labeled with 4′,6-diamidino-2-phenylindole (DAPI) for 10 min, and the cells were washed three more times with PBS. The fluorescence of DAPI and DOX were imaged with a confocal laser-scanning fluorescence microscope (CLSM, SP5, Leica, USA). The cellular uptake of the DOX-BSA/MnO_2 NPs was quantified by flow cytometry (FACSVerse, BD, US) to measure the DOX fluorescence. The acquired data were analyzed using FlowJo software (Version 7.6, Tree Star, Ashland, OR, US).

2.2.10. In vitro cell apoptosis detection

Cell apoptosis was detected using the Annexin V-APC/7-AAD Apoptosis Detection Kit. Briefly, 4T1 cells were seeded in a 6-well plate at a density of 3×10^5 cells/well. After overnight incubation, the medium was replaced with fresh medium containing free DOX, BSA/MnO_2 NPs or DOX-BSA/MnO_2 NPs. To obtain comparable data, the final concentrations of DOX and MnO_2 in all media containing these compounds were 5 μM and 100 μg/mL, respectively. After incubation at 37 °C under a 5% CO_2 atmosphere in the dark for 4 h, the cells in the laser treatment group were illuminated for 10 min with a 635-nm laser at a power density of 1.5 W/cm^2. After incubation for another 20 h, the cells were collected and washed three times with PBS. The cells were then detached using 0.25% (w/v) trypsin, resuspended in binding buffer, and labeled with Annexin V-APC and 7-AAD according to the manufacturer's instructions. The labeled cells were subsequently analyzed using a flow cytometer.

2.2.11. In vitro immunogenic cell death assays

The cell surface exposure of CRT was investigated for the detection of ICD. 4T1 cells were seeded in laser confocal dishes (15 mm in diameter) at a density of 1×10^5 cells/well and incubated overnight to allow cell attachment. After overnight incubation, the medium was replaced with fresh medium containing free DOX, BSA/MnO2 NPs or DOX-BSA/MnO2 NPs. To obtain comparable data, the final concentrations of DOX and MnO_2 NPs in all media containing these compounds were 5 μM and 100 μg/mL, respectively. After incubation in the dark at 37 °C under a 5% CO_2 atmosphere for 4 h, the cells in the laser treatment group were illuminated for 10 min with a 635-nm laser at a power density of 1.5 W/cm^2. The cells were then fixed with 4% paraformaldehyde solution, washed with PBS, incubated with Alexa Fluor 488-CRT antibody for 1 h at 4 °C, and further incubated with DAPI for 10 min. After three washes with PBS, the cells were observed under a CLSM. The fluorescence intensity of cells labeled with Alexa Fluor 488-CRT antibody was quantified by flow cytometry.

The release of ATP and HMGB-1 was also determined to evaluate the *in vitro* ICD. The contents of ATP and HMGB-1 within the cells were measured with an ATP content assay kit and an HMGB-1 enzyme-linked immunosorbent assay (ELISA) kit, respectively. Briefly, 4T1 cells were placed in 6-well plates (3×10^5 cells/well) and treated with DOX (5 μM), BSA/MnO_2 NPs (MnO_2 dose of 100 μg/mL) or DOX-BSA/MnO_2 NPs (DOX dose of 5 μM, MnO_2 dose of 100 μg/mL). After incubation in the dark for 4 h, the cells in the laser treatment group were illuminated for 10 min with a 635-nm laser at a power density of 1.5 W/cm^2. The cells were then collected and fully lysed to measure the concentrations of ATP and HMGB-1 according to the manufacturers' instructions.

2.2.12. Subcutaneous tumor models

All of the *in vivo* experiments were performed based on the guidelines of the Institutional Animal Care and Use Committee of 900 Hospital of the Joint Logistics Team (Fuzhou, China) and the Regulations for the Administration of Affairs Concerning Experimental Animals. Female BALB/c mice were used to build a 4T1 subcutaneous tumor model for *ex vivo* imaging, *in vivo* antitumor therapy, and *in vivo* safety assessment. The mice were subcutaneously injected in the left flank region with 1×10^6 cells suspended in 100 μL of PBS. The tumor volume was measured using the following formula: $V = (W^2 \times L)/2$, where V is the tumor volume, W is the width and L is the length of the tumor. The relative tumor volume was defined as V/V_0, where V_0 represents the initial volume before treatment.

2.2.13. In vivo fluorescence imaging and biodistribution

The tumor-bearing BALB/c mice were randomly divided into two groups. One hundred microliters of ICG solution or ICG-labeled BSA/MnO_2 NPs (ICG-BSA/MnO_2 NPs) was then administered *via* the tail vein at a dose of 1 mg/kg ICG. The mice were imaged using a living body imaging system (AniView 100, Biolight Biotechnology Co., Ltd., Guangzhou, China) equipped with fluorescent filter sets (excitation/emission, 740/820 nm) at predetermined time points (0.5, 1, 2, 4, 8, and 24 h after administration). The mice were sacrificed 24 h postinjection, and the hearts, livers, spleens, lungs, kidneys, and tumors were collected. The major organs were imaged by a living body imaging system under the same conditions.

2.2.14. In vivo antitumor efficacy

Once the tumor volume reached approximately 100 mm^3, the 4T1 tumor-bearing mice were randomly divided into 7 groups (n = 6): (1) saline, (2) saline plus laser irradiation, (3) DOX, (4) BSA/MnO_2 NPs, (5) BSA/MnO_2 NPs plus laser irradiation, (6) DOX-BSA/MnO_2 NPs and (7) DOX-BSA/MnO_2 NPs plus laser irradiation. All these formulations were administered through intravenous injection, and the DOX and MnO_2 NPs were administered at doses of 1 mg/kg and 0.5 mg/kg per mouse,

respectively, which were determined according to our results from a pre-experiment and some reports (Zhou et al., 2020; Chao et al., 2020) In addition, 1 h after administration, each mouse in the laser-treated group was irradiated for 10 min with a 635-nm laser at a power density of 1.5 W/cm^2. An infrared thermal camera was used to monitor the temperature change, and a thermal image of the whole mouse was recorded. The mice were i.v. injected with the above formulations on days 1, 4, and 7, and the tumor volume and body weight were measured and recorded every 2 days for 15 days. On the 15th day, all the mice were sacrificed, and the tumors were collected, weighed and examined by TdT-mediated dUTP nick-end labeling (TUNEL) staining. All the major organs (i.e., hearts, livers, spleens, lungs and kidneys) and the tumors were collected and detected by hematoxylin and eosin (H&E) staining.

To examine the immune response induced by the combinational therapy, the tumors were surgically resected from mice in the different groups. Briefly, for HIF-1α evaluation, the tumor tissues were cut into small pieces and stained with HIF-1α antibody according to the manufacturer's protocols. For TAM evaluation, the tumor tissues were cut into small pieces and placed into a glass homogenizer containing PBS solution (pH 7.4). A single-cell suspension was prepared by gentle pressure with a homogenizer (Takahashi et al., 2001). The cells were then stained with fluorescence-labeled antibodies, including CD45-PerCP-Cy5.5, CD11b-FITC, F4/80-PE, CD11c-PE-Cy7, and CD206-Alexa 647 antibodies, according to the manufacturer's protocols. CD45+CD11b+F4/80+CD11c+ and CD45+CD11b+F4/80+CD206+ cells were defined as M1- and M2-type TAMs, respectively. The gating strategies are presented in Supplementary Fig. S10. Serum was also collected from the mice to measure the TNF-α and IL-10 levels using a cytometric bead array (CBA) kit. The tumor tissues were then rapidly frozen in liquid nitrogen, sliced into 3-mm cryosections (Cryostat CM1950; Leica Microsystem) and stained with anti-mouse CD4 (with FITC-labeled goat anti-mouse as the secondary antibody), anti-mouse CD8 (with CY3-labeled goat anti-mouse as the secondary antibody) and anti-mouse Foxp3+ (with CY3-labeled goat anti-mouse as the secondary antibody) antibodies to evaluate the effect of immunotherapy.

2.2.15. *In vivo antitumor assessment using the bilateral tumor model*

To investigate the abscopal therapeutic effect on distant tumors, a bilateral tumor model was developed. For primary tumor inoculation, 4T1 cells (1×10^6) suspended in PBS were subcutaneously injected into the left flank of each female BALB/c mouse. Once the tumor volume reached approximately 100 mm^3 (day 0), the mice were randomly divided into 6 groups (n = 6), which were treated with (1) saline, (2) DOX, (3) BSA/MnO_2 NPs, (4) BSA/MnO_2 NPs plus laser irradiation, (5) DOX-BSA/MnO_2 NPs or (6) DOX-BSA/MnO_2 NPs plus laser irradiation and further treated as described in section 2.2.14. After the three treatments, distant tumors were introduced by injecting 4T1 cells (3×10^5) suspended in PBS into the right flank of each female BALB/c mouse on day 8. The distant tumor volume was then recorded until the end of the experiment, and the tumors were then harvested and used for immunofluorescence analyses of CD4+, CD8+ and Foxp3+ expression.

2.2.16. *Statistical analysis*

All the analysis data are provided as the means ± SDs. Student's *t* test was used to compare the results between two groups. Multiple-group comparisons were analyzed by one-way ANOVA. $^{\star}P > 0.05$ was considered to indicate a nonsignificant difference compared with the corresponding control, whereas $^{*}P < 0.05$ indicated a significant difference, and $^{**}P < 0.01$ and $^{***}P < 0.001$ indicated highly significant differences.

3. Results and discussion

3.1. *Preparation and characterization of nanoparticles*

Cancer is a disease characterized by uncontrolled cell proliferation that arises due to the accumulation of multiple genetic and somatic mutations in genes (proto-oncogenes and tumor suppressor genes) that regulate cell proliferation and apoptosis. Due to intratumor heterogeneity, tumor cells exhibit genetic diversity and drug resistance, which results in the need for very complex treatment processes and paradigms (Rahman et al., 2012). Nanoparticles that integrate multiple treatment paradigms are novel technological innovations developed recently to combat cancer and constitute the most effective approach for addressing the molecular heterogeneity and adaptive resistance found in cancer cells. This approach reduces the problems associated with conventional nanodrugs with respect to diagnosis, imaging and real-time controlled drug release and thus leads to reduced toxicity and a shorter treatment duration (Gindy and Prud'homme, 2009; Ahmad et al., 2019; Sau et al., 2018).

Because albumin is nontoxic and well tolerated by the immune system, it has attracted considerable interest as a component for drug carriers (Elsadek and Kratz, 2012). Considering its low cost, BSA has been widely studied as a component of nanocarriers in the field of nano-antitumor immunity instead of human serum albumin (Zhu et al., 2020; Zhou et al., 2021; He et al., 2020). The BSA/MnO_2 NPs were easily synthesized through an *in situ* redox reaction involving the simple mixing of $KMnO_4$ and BSA solutions for 1 h. BSA with reduced amino acid residues performed the dual roles of reductant and template in this preparation. $KMnO_4$ was reduced to MnO_2 around these active groups and grew gradually on BSA; resulting in the formation of BSA-templated MnO_2 NPs until the solution color changed from fuchsia to brown. The BSA/MnO_2 NPs were brown, whereas the DOX-BSA/MnO_2 NPs were red–brown due to the loaded DOX (Fig. 1A). As shown in Table 1, the average dynamic sizes of the BSA/MnO_2 and DOX-BSA/MnO_2 NPs were 20.22 ± 1.35 nm and 32.50 ± 2.31 nm, respectively. Nanoparticles <100 nm in size could facilitate the passive targeting of drugs to tumors *via* the enhanced permeability and retention (EPR) effect (Petros and DeSimone, 2010). The zeta potentials of the BSA/MnO_2 and DOX-BSA/MnO_2 NPs were −12.92 ± 2.16 mV and −26.80 ± 0.70 mV, respectively. The decrease in the zeta potential of the DOX-BSA/MnO_2 NPs was probably due to the loading of DOX·HCl. The EE% and LE% of DOX in the BSA/MnO_2 NPs were determined to equal 99.33 ± 0.09% and 23.88 ± 0.28%, respectively, and these values were comparable to those of commonly used DOX carriers such as mesoporous silica (Zhao et al., 2018), PLGA nanoparticles (Maksimenko et al., 2019), and block copolymer micelles (Alibolandi et al., 2015). The high EE% and LE% of DOX were probably due to the coordination between Mn and the anthraquinone rings of DOX (Zhang et al., 2017).

TEM images (Fig. 1B and Fig. 1C) showed that both the BSA/MnO_2 and DOX-BSA/MnO_2 NPs were uniformly dispersed spherical nanoparticles. Furthermore, the X-ray photoelectron spectroscopy (XPS) spectrum (Fig. 1D) showed two peaks at 654.2 and 642.4 eV, which were assigned to the Mn(IV) $2p_{1/2}$ and Mn(IV) $2p_{3/2}$ spin–orbit peaks of MnO_2, respectively (Gao et al., 2019). The concentrations of Mn^{4+} in the BSA/MnO_2 and DOX-BSA/MnO_2 NPs measured by ICP–OES were 801.47 ± 32.46 ppm and 396.90 ± 11.88 ppm, respectively.

The successful preparation of the DOX-BSA/MnO_2 NPs was also confirmed by UV–vis spectroscopy (Fig. 1E). The characteristic absorption peaks of DOX and the BSA/MnO_2 NPs appeared in the spectra of the DOX-BSA/MnO_2 NPs, which indicated that DOX was successfully loaded on the BSA/MnO_2 NPs. Incubation of the DOX-BSA/MnO_2 NPs with saline containing 10% FBS for 7 days at 37 °C barely changed the particle size and PDI, indicating good stability (Fig. S1). Moreover, the particles exhibited good stability even after exposure to laser irradiation (1.5 W/cm^2, 635 nm) for 10 min, as demonstrated by the finding that the particle size and PDI remained stable over 7 days (Fig. S1).

3.2. *In vitro photothermal effect*

Inspired by the strong UV–vis absorbance of the BSA/MnO_2 NPs and DOX-BSA/MnO_2 NPs, we further investigated the photothermal effect of

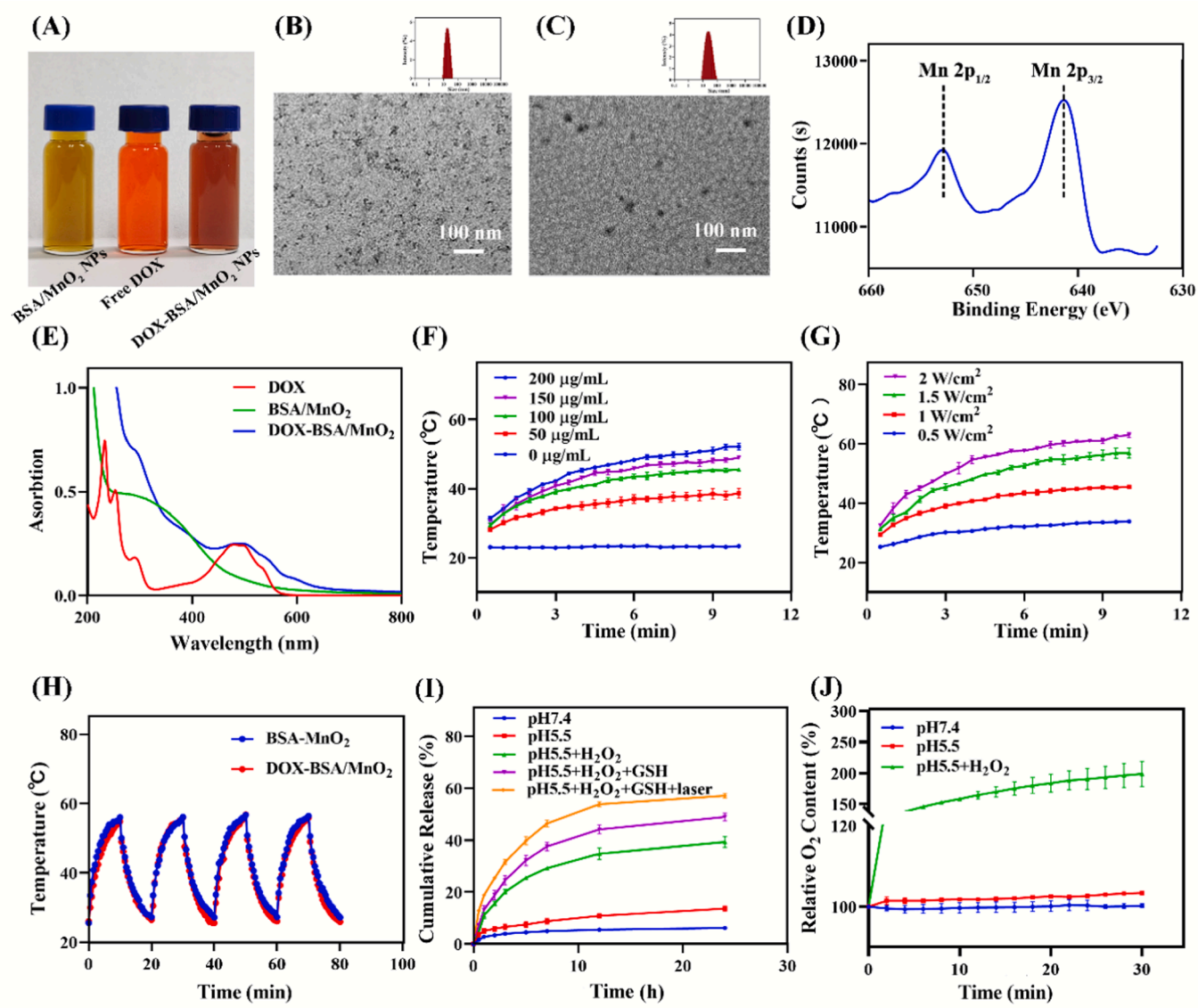

Fig. 1. Nanoparticle characterization. (A) Photographs of nanoparticles. TEM images of the (B) BSA/MnO_2 NPs and (C) DOX-BSA/MnO_2 NPs. (D) XPS spectrum of the DOX-BSA/MnO_2 NPs. (E) UV–vis spectra of free DOX, BSA/MnO_2 NPs, and DOX-BSA/MnO_2 NPs. (F) Change in the temperature of the BSA/MnO_2 NPs in water at various concentrations under irradiation with a 635-nm laser at a power density of 1.0 W/cm^2, n = 3. (G) Change in the temperature of the BSA/MnO_2 NPs in water (MnO_2 dose of 100 μg/mL) under 635-nm laser irradiation at different power densities, n = 3. (H) Temperature cycling stability of the BSA/MnO_2 and DOX-BSA/MnO_2 NPs under 1.5-W/cm^2 irradiation for four on/off cycles (10 min of irradiation for each cycle). (I) Cumulative release of DOX from the DOX-BSA/MnO_2 NPs under different conditions with laser exposure for 10 min. (J) Oxygen generation from the DOX-BSA/MnO_2 NPs under different conditions.

Table 1
Characterization of nanoparticles (n = 3).

Preparation	Diameter	PDI	Zeta potential (mV)	EE (%)	LE (%)
BSA/MnO_2	20.22 ± 1.35	0.220 ± 0.170	−12.92 ± 2.16	–	–
DOX-BSA/MnO_2	32.50 ± 2.31	0.240 ± 0.006	−26.80 ± 0.70	99.33 ± 0.09	23.88 ± 0.28

these nanoparticles. The BSA/MnO_2 NPs in solution and DOX-BSA/MnO_2 NPs in solution were exposed to 635-nm laser irradiation for 10 min at different concentrations and laser power densities. Purified water was used as a negative control. An IR thermal camera was used to monitor the temperature variation. As shown in Fig. 1F and 1G, the temperature of the BSA/MnO_2 NP solution increased with increases in the irradiation time, laser power density and nanoparticle concentration. In comparison, the temperature of purified water hardly changed (Fig. S2). In particular, under a power density of 1.5 W/cm^2 for 10 min, the temperature of the BSA/MnO_2 NP solution (MnO_2 dose of 100 μg/mL) increased from room temperature to 56.9 °C, which meets the requirements for hyperthermia-induced ICD (Habash et al., 2006). Therefore, a dose of 100 μg/mL and a laser power density of 1.5 W/cm^2 were used for further photothermal studies. Moreover, no significant differences in photothermal effects were found between the BSA/MnO_2 NPs and DOX-BSA/MnO_2 NPs (Fig. S3).

In addition to good photothermal conversion performance, the photostability of nanoparticles is another important element that needs to be further investigated. For this purpose, the BSA/MnO_2 NP solution was irradiated through four continuous laser on/off cycles. As shown in Fig. 1H, the photothermal effect of the BSA/MnO_2 NPs did not change during the four on–off cycles of irradiation, which indicated their excellent photothermal stability. The BSA/MnO_2 NPs and DOX-BSA/MnO_2 NPs exhibited almost overlapping temperature change curves

throughout the irradiation process, which indicated that the loading of DOX did not affect the photothermal stability of the BSA/MnO_2 NPs. The photothermal conversion efficiencies of the BSA/MnO_2 NPs and DOX-BSA/MnO_2 NPs were 27.71% and 27.79% (Fig. S4 and Table S1), respectively. Moreover, according to previous research, the good photothermal effect of the DOX-BSA/MnO_2 NPs was due to MnO_2 itself (Liu et al., 2018). Taken together, these results indicated that BSA/MnO_2 NPs exhibited desirable photothermal efficiency and photostability and could be employed as ideal photothermal agents for tumor therapy.

3.3. In vitro DOX release

MnO_2 is reportedly decomposed in acidic environments enriched with H_2O_2 and GSH, which is a distinctive feature of solid tumors (Yu et al., 2019; Fan et al., 2016). Therefore, we investigated the cumulative release behaviors of DOX from the DOX-BSA/MnO_2 NPs in various aqueous solutions (Fig. 1I). Compared with the slow release of DOX from the DOX-BSA/MnO_2 NPs at pH 7.4 (6.14 ± 0.45% within 24 h), DOX release was effectively accelerated (13.71 ± 0.91% within 24 h) in a mildly acidic solution (pH 5.5) due to the faster decomposition of MnO_2 under weakly acidic conditions. Furthermore, faster DOX release (39.37 ± 2.17% within 24 h) was achieved with the addition of H_2O_2, which indicated that H_2O_2 could accelerate the degradation of MnO_2 under weakly acidic conditions. Noticeably, the fastest release of DOX from the DOX-BSA/MnO_2 NPs (48.96 ± 1.45%) was observed under weakly acidic conditions in the presence of GSH and H_2O_2, which was attributed to the accelerated degradation of MnO_2 by both GSH and H_2O_2. Interestingly, with laser irradiation, the release of DOX was greatly accelerated (57.11 ± 0.89% within 24 h *versus* 48.96 ± 1.45% within 24 h), which was consistent with a previous report that photothermal irradiation could promote the release of DOX from nanoparticles (Wang et al., 2016). In conclusion, all of these results demonstrated that the DOX-release behavior of the DOX-BSA/MnO_2 NPs favored the site-specific release of DOX in the TME and thereby resulted in reduced undesired side effects on normal tissues (Liang et al., 2014).

3.4. In vitro O_2 production

Considering the overexpression of H_2O_2 (10–100 μM) inside most types of solid tumors and the catalase-like activity of MnO_2-based nanoparticles (Chen et al., 2016), we determined the ability of the DOX-BSA/MnO_2 NPs to catalyze the decomposition of H_2O_2 into O_2 using a

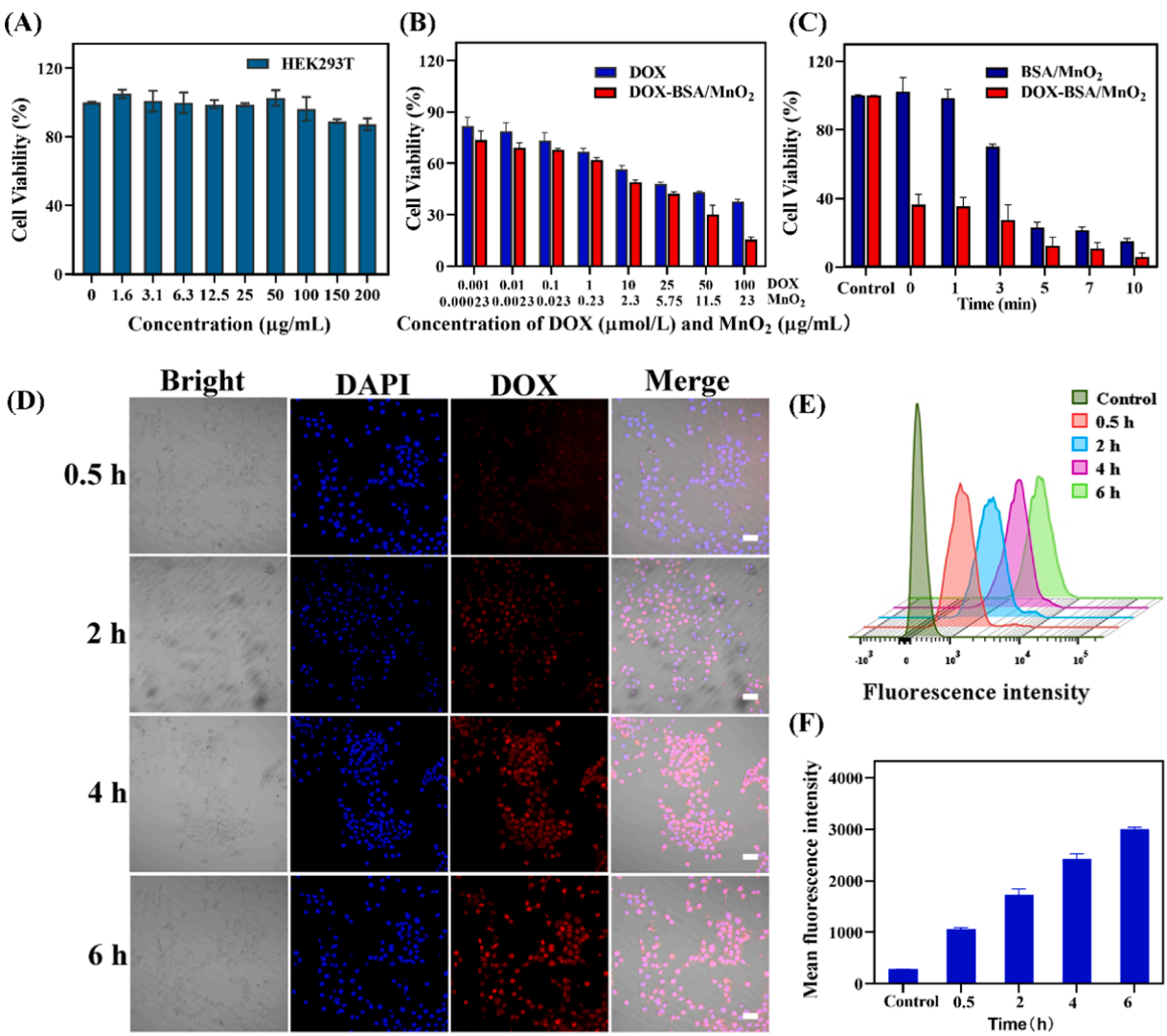

Fig. 2. (A) Cell viability of HEK293T cells treated with the BSA/MnO_2 NPs, n = 6. (B) Viability of 4T1 cells treated with DOX and DOX-BSA/MnO_2 NPs at various concentrations, n = 6. (C) Cell viability of 4T1 cells treated with the BSA/MnO_2 NPs and DOX-BSA/MnO_2 NPs under 635-nm laser irradiation (1.5 W/cm^2) for various times (DOX dose of 5 μM, MnO_2 dose of 100 μg/mL), n = 6. (D) Cellular uptake of the DOX-BSA/MnO_2 NPs by 4T1 cells at different time points (scale bar = 20 μm). Flow cytometry was used to quantify the uptake of the DOX-BSA/MnO_2 NPs by the cells. n = 3. (E) Overlay of fluorescence intensity data obtained by flow cytometry. (F) Mean fluorescence intensity of 4T1 cells incubated with the DOX-BSA/MnO_2 NPs for 0.5, 2, 4, and 6 h.

portable dissolved oxygen meter. As shown in Fig. 1J, under concurrent stimulation by H^+ (pH 5.5) and H_2O_2 (100 μM), the DOX-BSA/MnO_2 NPs generated O_2 quickly, whereas the O_2 concentration did not increase in the absence of the DOX-BSA/MnO_2 NPs. These results indicated that the DOX-BSA/MnO_2 NPs can generate O_2 using H_2O_2 as a feedstock and have the potential to alleviate tumor hypoxia.

3.5. Cytotoxicity of the BSA/MnO_2 NPs

The cytotoxicity of the BSA/MnO_2 NPs was determined by the MTT assay. As shown in Fig. S5 and Fig. 2A, in the presence of BSA/MnO_2 NPs at a concentration as high as 200 μg/mL, the survival rates of LO2 cells (human normal hepatocyte cell line) and HEK 293T cells (human embryonic kidney cell line) were 82.41 ± 2.60% and 87.32 ± 3.57%, respectively, which indicated the low cytotoxicity of the BSA/MnO_2 NPs in normal cells (Zhang et al., 2018).

3.6. Antitumor cytotoxicity

To evaluate whether the DOX-BSA/MnO_2 NPs affected the cytotoxicity of DOX, the cell viability of 4T1 cells after 24 h of exposure to free DOX and DOX-BSA/MnO_2 NPs was investigated. As shown in Fig. 2B,

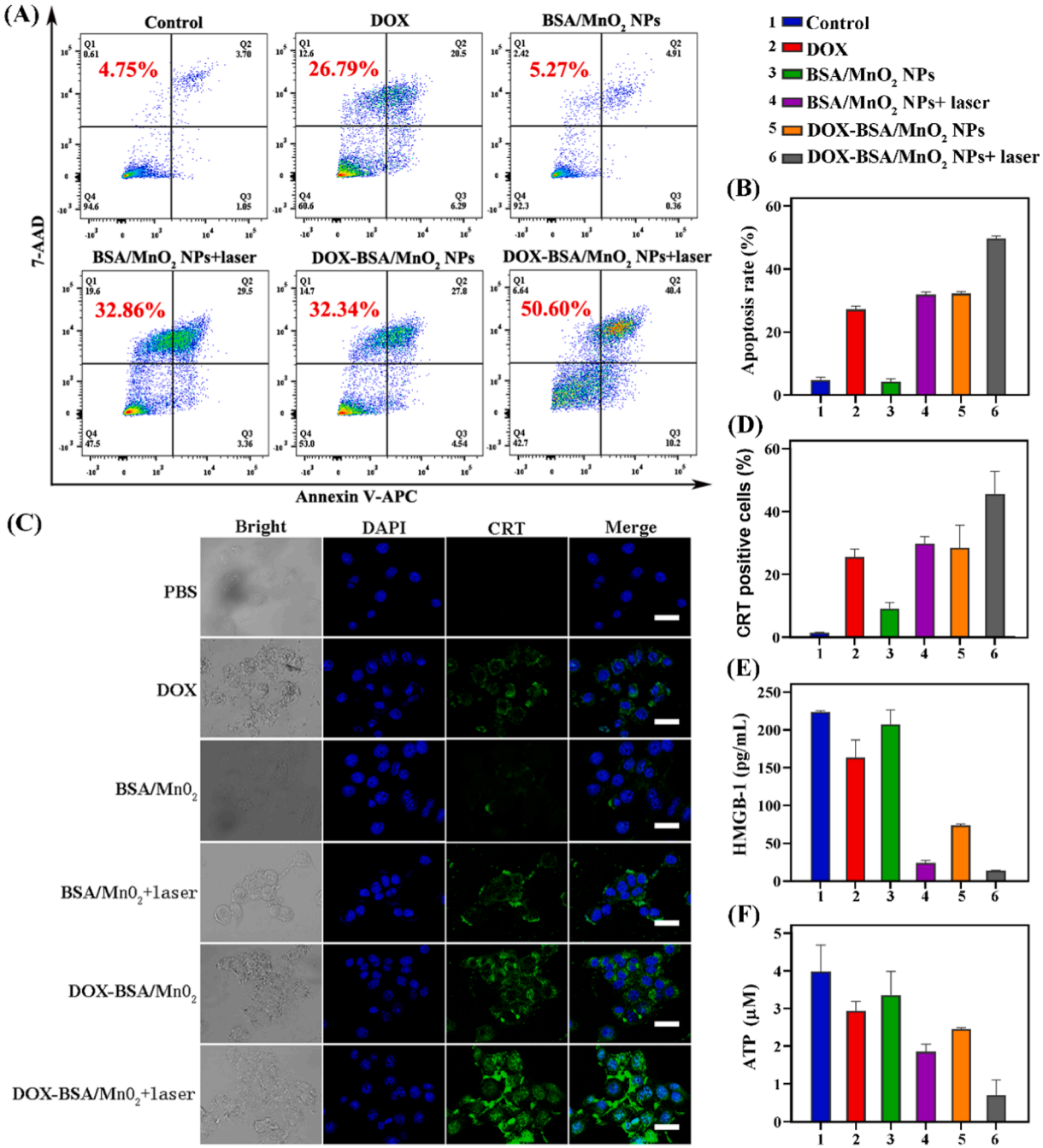

Fig. 3. *In vitro* antitumor effect of nanoparticles and *in vitro* ICD induction. (A) Flow cytometry analysis of 4T1 cells with Annexin V-APC/7-AAD double staining after treatment with DOX, BSA/MnO_2 NPs, BSA/MnO_2 NPs+ laser, DOX-BSA/MnO_2 NPs and DOX-BSA/MnO_2 NPs+ laser. (B) Quantitative analysis of the apoptosis rate, n = 3. (C) CLSM fluorescence images (scale bar = 20 μm) of CRT exposure by 4T1 cells treated with DOX, BSA/MnO_2 NPs, BSA/MnO_2 NPs+ laser, DOX-BSA/MnO_2 NPs and DOX-BSA/MnO_2 NPs+ laser. (D) Flow cytometry analysis of CRT exposure on the cell surface of 4T1 cells. Intracellular concentrations of (E) HMGB-1 and (F) ATP.

both free DOX and DOX-BSA/MnO_2 NPs inhibited the proliferation of 4T1 cells in a dose-dependent manner, and the IC50 value of the DOX-BSA/MnO_2 NPs (12.9 μM, Fig. S6) against 4T1 cells was markedly lower than that of free DOX (27.5 μM, Fig. S7), which indicated that the DOX-BSA/MnO_2 NPs could effectively enhance the cytotoxicity of DOX.

To investigate whether DOX-BSA/MnO_2 NP-mediated chemo-photothermal therapy could synergistically inhibit the proliferation of tumor cells, the proliferation of 4T1 cells treated with different formulations was assessed by the MTT assay. After incubation with the BSA/MnO_2 NPs or DOX-BSA/MnO_2 NPs for 4 h, 4T1 cells were exposed to 635-nm laser irradiation at a power density of 1.5 W/cm^2 for different time periods. As shown in Fig. 2C, compared with photothermal therapy (PTT) alone (BSA/MnO_2 NPs plus laser irradiation) or chemotherapy alone (DOX-BSA/MnO_2 NPs without laser irradiation), the combination therapy (DOX-BSA/MnO_2 NPs plus laser irradiation) was found to be more synergistically effective in killing 4T1 cells. Moreover, with increases in the irradiation time, a marked decrease in cell viability was observed after treatment with DOX-BSA/MnO_2 NPs plus laser irradiation. In summary, we confirmed that the DOX-BSA/MnO_2 NPs exerted a synergistic effect in PTT combined with chemotherapy.

3.7. In vitro cell uptake

The intracellular accumulation of DOX-BSA/MnO_2 NPs in 4T1 cells was investigated with a CLSM. As shown in Fig. 2D, the DOX-BSA/MnO_2 NPs entered cells rapidly: DOX fluorescence (red fluorescence) rapidly appeared in the nucleus (observed after incubation for 0.5 h), and the fluorescence intensity inside cell nuclei increased significantly over time, indicating the time-dependent uptake of the DOX-BSA/MnO_2 NPs by 4T1 cells. The mean fluorescence intensity of these fluorescence images was also calculated quantitatively by flow cytometry (Fig. 2E and F). The above-described results suggested the gradual intracellular release of DOX from the DOX-BSA/MnO_2 NPs after the breakup of MnO_2 nanocarriers within acidic lysosomes.

3.8. Cell apoptosis detection

An Annexin V-APC/7-AAD Apoptosis Detection Kit was used to detect the major death pathway of 4T1 cells after treatment with the DOX-BSA/MnO_2 NPs by flow cytometry. As illustrated in Fig. 3A and B, only 5.27% apoptotic cells were observed after treatment with the BSA/MnO_2 NPs alone, indicating good biocompatibility. Notably, the apoptosis ratio of the 4T1 cells treated with the BSA/MnO_2 NPs plus laser irradiation was significantly increased to 32.86%, which indicated the good photothermal effects of the BSA/MnO_2 NPs. In addition, 32.34% of 4T1 cells were apoptotic after treatment with the DOX-BSA/MnO_2 NPs, whereas only 26.79% of 4T1 cells were apoptotic after treatment with free DOX. These results indicated that the DOX-BSA/MnO_2 NPs could enhance the cytotoxicity of DOX. The DOX-BSA/MnO_2 NPs combined with laser irradiation induced the highest cell apoptosis rate (approximately 50.60%), which demonstrated that chemo-photothermal therapy could synergistically induce apoptosis in 4T1 cells. These results were in good agreement with the results from the cell viability assay.

3.9. In vitro ICD assays

ICD is defined as a cell death modality that stimulates an immune response against dead-cell antigens (Kroemer et al., 2013). It has been reported that either DOX or PTT can elicit ICD, and the combination of the two can induce stronger ICD (Bezu et al., 2015). Because treatment with the DOX-BSA/MnO_2 NPs plus laser irradiation was capable of performing the dual functions of DOX and PTT, the ability of the NPs to synergistically trigger ICD to generate DAMPs was evaluated. As shown in Fig. 3C, CLSM imaging revealed that all the groups with the exception of the control group were able to induce different degrees of CRT exposure on the surface of 4T1 cells, and the BSA/MnO_2 NP treatment group exhibited the least CRT exposure. The DOX-BSA/MnO_2 NP treatment group exhibited a higher degree of CRT exposure than the free DOX treatment group. The DOX-BSA/MnO_2 NPs plus laser irradiation treatment group showed a higher degree of exposure than the DOX-BSA/MnO_2 NP treatment group (chemotherapy alone) or BSA/MnO_2 NP plus laser irradiation treatment group (PTT alone), which indicated that chemo-photothermal therapy could synergistically elicit a higher degree of CRT exposure than monotherapy. The CRT surface exposure of 4T1 cells after these treatments was quantitatively confirmed by flow cytometry, which showed the same trend as that obtained with the CLSM (Fig. 3D).

ATP and HMGB-1 migrate out of tumor cells that undergo ICD (Galluzzi et al., 2020). Accordingly, the contents of intracellular ATP and HMGB-1 were measured to evaluate the extent of ICD (Feng et al., 2020; Lv et al., 2021). As illustrated in Fig. 3E and 3F, the DOX-BSA/MnO_2 NP plus laser irradiation treatment group exhibited lower intracellular ATP and HMGB-1 levels, which was consistent with the conclusions from the CRT exposure analysis, and these results indicated that the simultaneous combination of DOX and PTT could synergistically induce a higher degree of ICD than either the DOX-BSA/MnO_2 NP treatment (chemotherapy alone) or the BSA/MnO_2 NP plus laser irradiation treatment (PTT alone). Interestingly, the BSA/MnO_2 NPs could also induce the production of ATP and HMGB-1, which reinforced the notion that the BSA/MnO_2 NPs could act as ICD drugs in tumor immunotherapy (Ding et al., 2020).

3.10. In vivo fluorescence imaging and biodistribution

To determine the optimal laser irradiation time and investigate the targeting ability of nanoparticles, *in vivo* fluorescence imaging was performed. The BSA/MnO_2 NPs were labeled with ICG (1 mg/kg) (ICG-BSA/MnO_2 NPs), and an equal dose of free ICG was used as a control (Pan et al., 2018). As shown in Fig. 4A and B, the ICG fluorescence intensity of the ICG-BSA/MnO_2 NPs in the tumor region peaked at 1 h postinjection, and the fluorescence signal could be detected even at 24 h postinjection. In contrast, after the injection of free ICG, the fluorescence intensity of free ICG decreased rapidly over time, and the fluorescence signal had almost disappeared at 4 h postinjection. The *ex vivo* imaging of major organs (hearts, livers, spleens, lungs and kidneys) and tumors collected 24 h postinjection indicated high tumor enrichment of the ICG-BSA/MnO_2 NPs and rapid *in vivo* clearance of ICG (Fig. 4C and D). Notably, strong DOX-BSA/MnO_2 NP fluorescence was found in the kidneys at 24 h postinjection, which was due to the dissociation of the nanoparticles into small individual albumin for renal clearance (Tian et al., 2017; Zhou et al., 2021) Therefore, ICG-BSA/MnO_2 NPs could accumulate in tumor tissues more efficiently than free ICG, and the optimal treatment time for PTT appeared to be 1 h postinjection.

3.11. DOX-BSA/MnO_2 NP-mediated combinational therapy to inhibit the growth of primary tumors

We used mice bearing the triple-negative breast tumor cell line 4T1 to validate whether DOX-BSA/MnO_2 NP-mediated combinational therapy could effectively inhibit the growth of primary tumors. Once the tumor volumes reached ~100 mm^3, the 4T1 tumor-bearing BALB/c mice were randomly grouped, and each group was treated with saline, saline plus laser irradiation, DOX, BSA/MnO_2 NPs, BSA/MnO_2 NPs plus laser irradiation, DOX-BSA/MnO_2 NPs, or DOX-BSA/MnO_2 NPs plus laser irradiation on days 1, 4, and 7 postinjection, as shown in Fig. 5A. For each group, the doses of DOX and MnO_2 were 1.0 mg/kg and 0.5 mg/kg, respectively. Timed NIR irradiation with a 635-nm laser (1.5 W/cm^2, 10 min) was applied to the mice in the laser treatment group.

First, the photothermal conversion of the BSA/MnO_2 NPs and DOX-BSA/MnO_2 NPs was evaluated by infrared thermal imaging. As shown in Fig. 5B and C, under 635-nm laser irradiation, the surface temperature

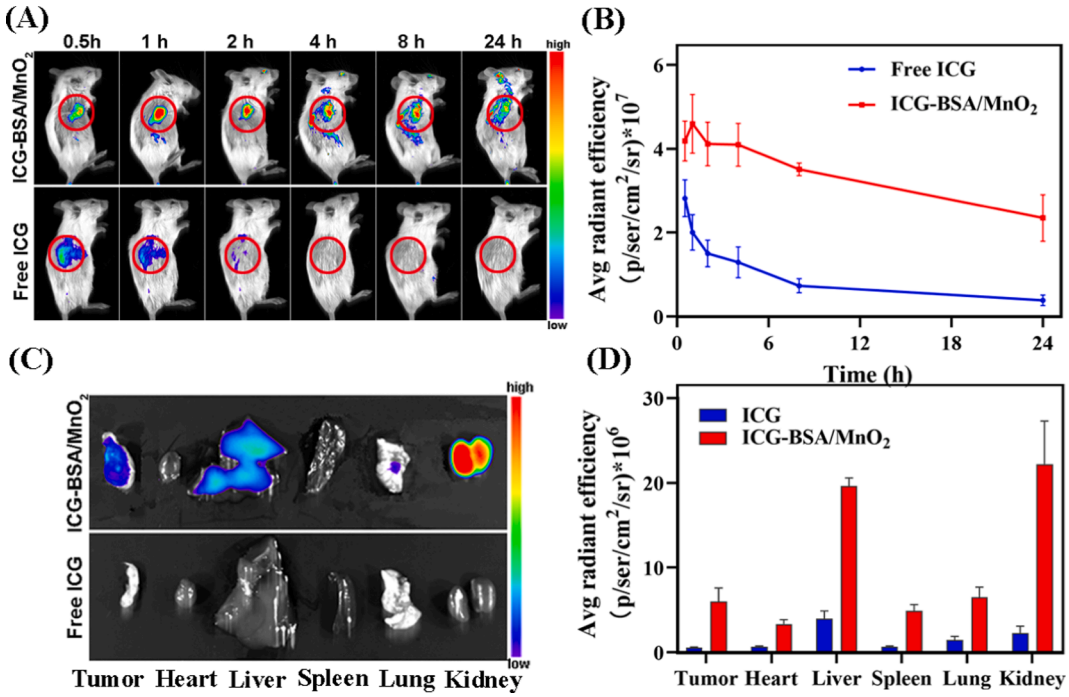

Fig. 4. Biodistribution of the ICG-BSA/MnO_2 NPs and free ICG after i.v. injection. (A) Fluorescence imaging of 4T1-bearing BALB/c mice at designated time points after i.v. injection of free ICG and ICG-BSA/MnO_2 NPs (the tumor area is circled in red). (B) Quantification of the fluorescence intensity of tumors in 4T1-bearing BALB/c mice at designated time points after i.v. injection of free ICG and ICG-BSA/MnO_2 NPs. (C) *Ex vivo* fluorescence images of tumors and major organs excised from 4T1-bearing BALB/c mice 24 h after injection of the ICG-BSA/MnO_2 NPs and free ICG. (D) Quantification of the *ex vivo* fluorescence intensity of tumors and major organs excised from 4T1-bearing BALB/c mice 24 h after injection of the ICG-BSA/MnO_2 NPs and free ICG. (For interpretation of the references to color in this figure legend, the reader is referred to the web version of this article.)

of the tumors administered the BSA/MnO_2 NPs and DOX-BSA/MnO_2 NPs exhibited a similar enhancement trend and reached approximately 60 °C within 10 min ($p > 0.05$), which was sufficiently high to cause cell ablation and elicit immune responses (Li et al., 2021), whereas only a weak heating effect was observed in the saline treatment group.

The inhibition of the growth of primary tumors by different formulations is shown in Fig. 5D and E. The observation of the DOX-BSA/MnO_2 NP plus laser irradiation group revealed that tumor growth was almost completely inhibited during the 15-day observation period. In contrast, tumor growth in the mice treated with DOX-BSA/MnO_2 NPs or BSA/MnO_2 NPs plus laser irradiation was inhibited but to a significantly lesser extent. These results suggested that DOX-BSA/MnO_2 NP-mediated combinational therapy was more efficient than monotherapy (PTT or chemotherapy). Moreover, the DOX-BSA/MnO_2 NP group showed better tumor growth inhibition than the DOX group, which suggested that the DOX-BSA/MnO_2 NPs could effectively enhance the tumor growth inhibition of DOX due to the better tumor targeting achieved by the DOX-BSA/MnO_2 NPs than by free DOX, as previously noted in section 3.10. The tumor sizes in both the saline and saline plus laser irradiation groups increased rapidly during the observation period, and no significant difference was found between these two groups, which was consistent with published work (Tang et al., 2016). In addition, TUNEL fluorescent staining was performed to investigate the mechanism of action of these formulations. As shown in Fig. 5F, tumors treated with the DOX-BSA/MnO_2 NPs plus laser irradiation emitted the brightest green-fluorescence signals, which indicated that the DOX-BSA/MnO_2 NPs plus laser irradiation group exhibited the maximal degree of cell apoptosis. This finding was consistent with the H&E staining results. Moreover, the relative body weights showed negligible changes until the end of the observation period (Fig. S8), which confirmed the safety of these formulations, and this finding was also verified by H&E staining of major organs (hearts, livers, spleens, lungs, and kidneys) collected from mice at the end of the experiment (Fig. S9).

3.12. Immunological responses after combined therapy

Encouraged by the results of *in vitro* ICD induction and the *in vivo* antitumor effects of DOX-BSA/MnO_2 NP-mediated combination therapy, we further evaluated their abilities to trigger immunological responses. Substantial evidence highlights the essential roles of TAMs in effective tumor immunotherapy (Pollard, 2004). For example, M1-type TAMs exhibit classic antitumor activity, whereas M2-type TAMs can promote tumor progression and metastasis by inhibiting antitumor immunity (Laoui et al., 2014). A previous study showed that the hypoxic TME can tune TAMs into M2-type phenotype cells and thereby weakens the antitumor immune response (Tang et al., 2019). Given the ability of DOX-BSA/MnO_2 NPs to generate O_2 in response to H_2O_2 in tumor cells, we first verified whether DOX-BSA/MnO_2 NPs could relieve tumor hypoxia. As shown in Fig. 6A, the expression level of HIF-1α in tumor tissues after saline plus laser irradiation or DOX treatment was almost the same as that after saline treatment, which indicated that neither saline plus laser irradiation treatment nor DOX treatment changed the expression of HIF-1α. The expression of HIF-1α in the BSA/MnO_2 NP- and DOX-BSA/MnO_2 NP-treated groups was lower than that in the saline-injected control group. The reason for this difference might be that the catalase-like activity of MnO_2 catalyzed the degradation of intracellular H_2O_2 into O_2 and thus relieved tumor hypoxia. Noticeably, among these treatments, the lowest expression of HIF-1α in tumor tissues was observed after treatment with DOX-BSA/MnO_2 NPs plus laser irradiation, probably because hyperthermia assisted MnO_2 in overcoming tumor hypoxia (Yang et al., 2017).

Subsequently, the hypoxia-regulated polarization of TAMs was investigated by flow cytometry. As shown in Fig. 6B, compared with the results obtained for the saline-treated group, the proportion of M1-type TAMs showed a clear increase from 15.3% to 50.7% in the mice treated with DOX-BSA/MnO_2 NPs plus timed irradiation with a 635-nm laser, and in contrast, the amount of M2-type TAMs decreased significantly

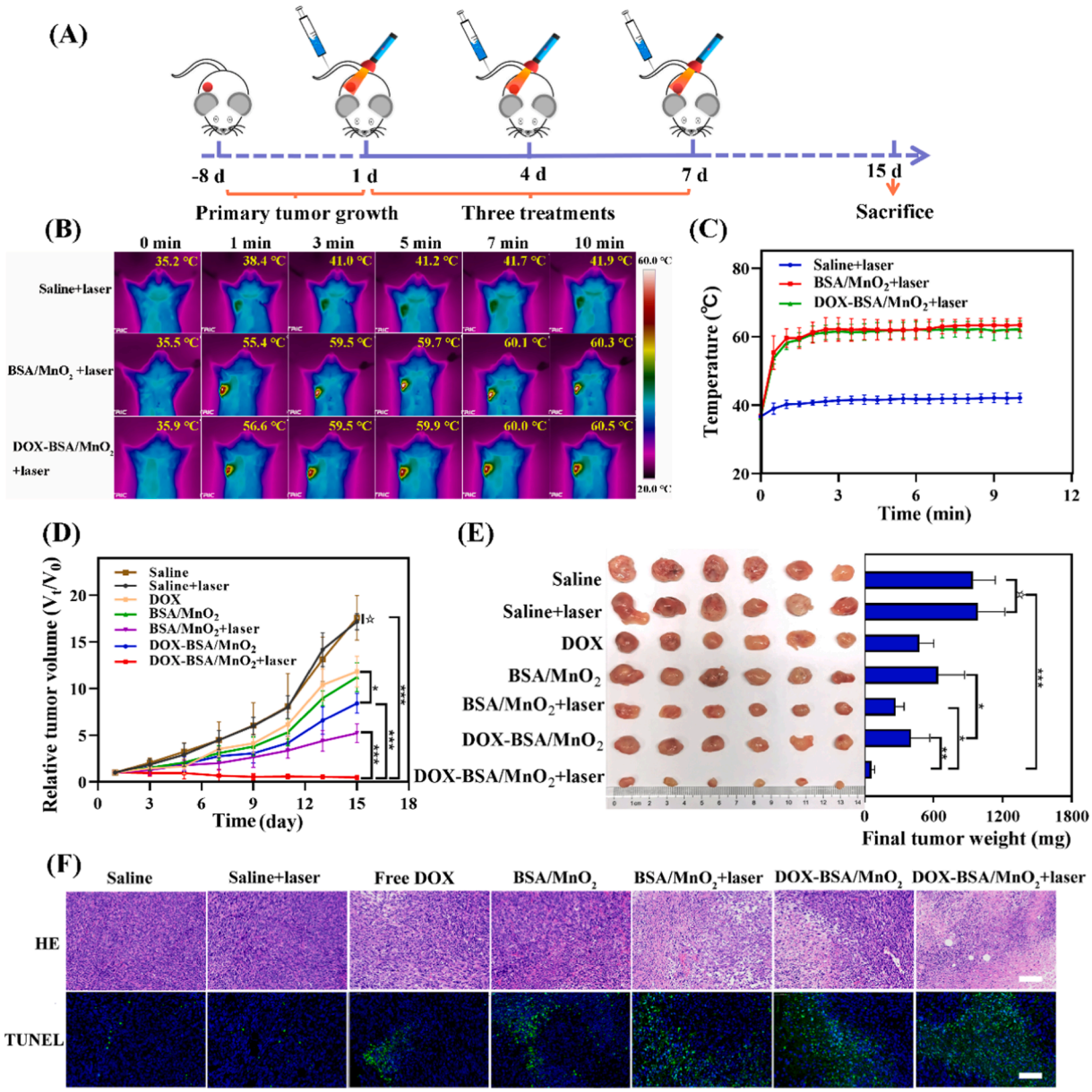

Fig. 5. Primary tumor inhibition assay. (A) Schematic illustration of the animal experimental design with 4T1-bearing BALB/c mice. (B) *In vivo* infrared thermal images of the tumor sites in 4T1-bearing BALB/c mice. Images were recorded after 0, 1, 3, 5, 7, and 10 min of irradiation. (C) Temperature variation curves of the tumor sites in 4T1-bearing BALB/c mice after i.v. injection with saline, BSA/MnO_2 NPs, and DOX-BSA/MnO_2 NPs and subsequent 635-nm laser irradiation (1.5 W/cm^2). (D) Tumor growth curves of the 4T1-bearing BALB/c mouse model, n = 6. (E) Images and weights of tumors obtained from 4T1-bearing BALB/c mice on the 15th day after treatment, n = 6. (F) H&E and TUNEL staining images of tumors collected from 4T1-bearing BALB/c mice on the 15th day after treatment (scale bar = 100 μm).

from 24.0% to 6.77%. The BSA/MnO_2 NP, DOX and DOX-BSA/MnO_2 NP treatments also induced a certain level of M1-type TAMs, although to a much smaller extent than the DOX-BSA/MnO_2 NP plus laser irradiation treatment. In contrast, no significant change in TAM phenotypes was observed in tumors after saline plus laser treatment. Moreover, the secretion of IL-10 (the predominant cytokine secreted by M2-type macrophages) in the supernatant of tumor lysates significantly decreased by 2.84 fold in the mice treated with the DOX-BSA/MnO_2 NPs plus laser irradiation (Fig. 6C) (Galon and Bruni, 2019), whereas the secretion of TNF-α, the predominant cytokine secreted by M1-type macrophages, increased by 3.42 fold (Fig. 6D) (Yuan et al., 2021). All these results indicated substantial M1-type TAM polarization after combined treatment with the DOX-BSA/MnO_2 NPs plus laser irradiation.

The hypoxic TME could also induce the upregulation of Tregs and the downregulation of tumor infiltrating lymphocytes, including cytotoxic T cells (CD8+ T cells), helper T cells (CD4+ T cells), and other immune cells, which play vital roles in antitumor immunotherapy (Vanneman and Dranoff, 2012; Kabingu et al., 2009). Therefore, we performed an immunofluorescence analysis to measure the populations of distinct subgroups of T cells in tumors after different types of treatments. The tumors treated with the DOX-BSA/MnO_2 NPs plus laser irradiation contained more CD4+ and CD8+ T cells than the tumors in the other groups (Fig. 6E). Moreover, treatment with the DOX-BSA/MnO_2 NPs plus laser irradiation significantly reduced the population of immunosuppressive Tregs within tumors compared with that in the saline treatment group. These notable effects may be attributed to the high TME modulation capacity of the DOX-BSA/MnO_2 NPs and the consequently enhanced ability of the treatment combined with chemo-photothermal therapy to induce the release of tumor-associated

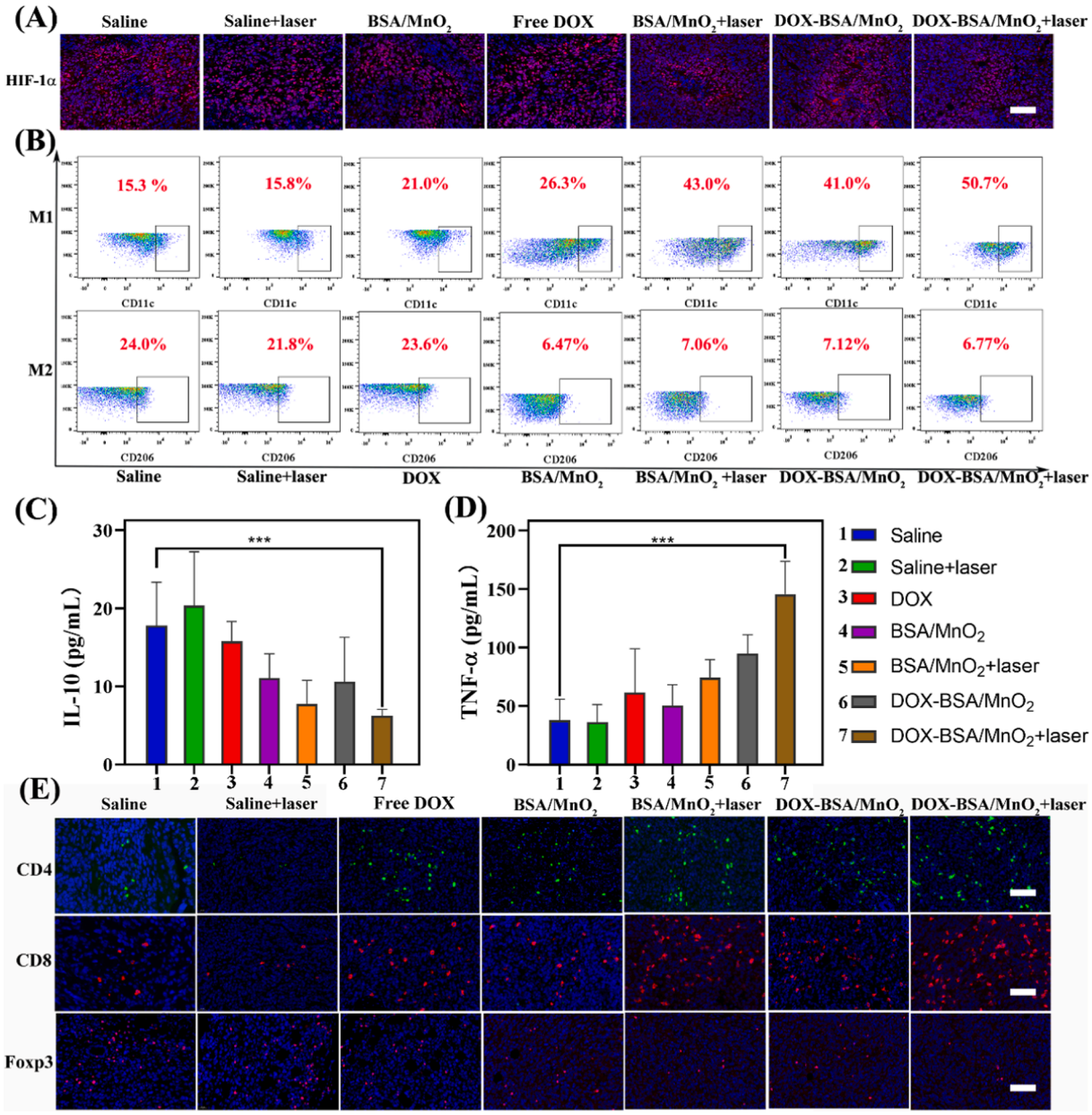

Fig. 6. Immune responses induced by the DOX-BSA/MnO_2 NPs plus laser irradiation. (A) Representative immunofluorescence images of HIF-1α in tumors on day 15 after the different treatments. The nuclei and hypoxic areas were stained with DAPI (blue) and HIF-1α antibody (red), respectively (scale bar = 100 μm). (B) Proportions and flow cytometry plots of CD11c+ (M1-type TAMs) and CD206+ (M2-type TAMs) cells in the tumors examined on day 15 after treatment. Concentrations of (C) IL-10 and (D) TNF-α in the plasma, n = 6. (E) Representative immunofluorescence images of tumor tissues stained with DAPI (blue), CD4+ (green), CD8+ (red) and Foxp3+ (red) in the different treatment groups (scale bar = 100 μm). (For interpretation of the references to color in this figure legend, the reader is referred to the web version of this article.)

antigens (Yang et al., 2021; Hafez et al., 2018), which activate DCs and thus promote the recruitment of cytotoxic T lymphocytes (CTLs) into tumors.

Many multifunctional MnO_2 nanoparticles reportedly regulate the TME and thus favor antitumor immune responses (Singh et al., 2013). However, compared with other MnO_2 nanoparticles, our system could regulate the TME more effectively with a very low dose of MnO_2 (0.5 mg/kg), preventing the toxicity of MnO_2 itself (Hafez et al., 2018; Singh et al., 2013). The reason might be that MnO_2-mediated hyperthermia aids MnO_2 in alleviating tumor hypoxia to a certain extent and thereby enhances the regulation of MnO_2 by the TME. In conclusion, in addition to killing tumor cells, the combination of chemotherapy and PTT performed with our DOX-BSA/MnO_2 nanoplatform synergistically induced CTL-mediated antitumor immunity and moderated the immunosuppressive TME to promote the immune killing of tumor cells that survived the first round of the combination treatment with chemo-photothermal therapy.

3.13. *DOX-BSA/MnO_2-mediated combinational therapy for inhibiting the growth of abscopal tumors*

Improving prognosis and inhibiting tumor recurrence are important factors in improving the effectiveness of tumor treatment (Chen et al., 2015). To further investigate whether the established antitumor immune responses triggered by the DOX-BSA/MnO_2 NPs plus laser irradiation were sufficiently strong to inhibit an untreated distant tumor, a distant tumor model was established and observed after treatment of the primary tumors (Fig. 7A). As shown in Fig. 7B, the changes in the size e

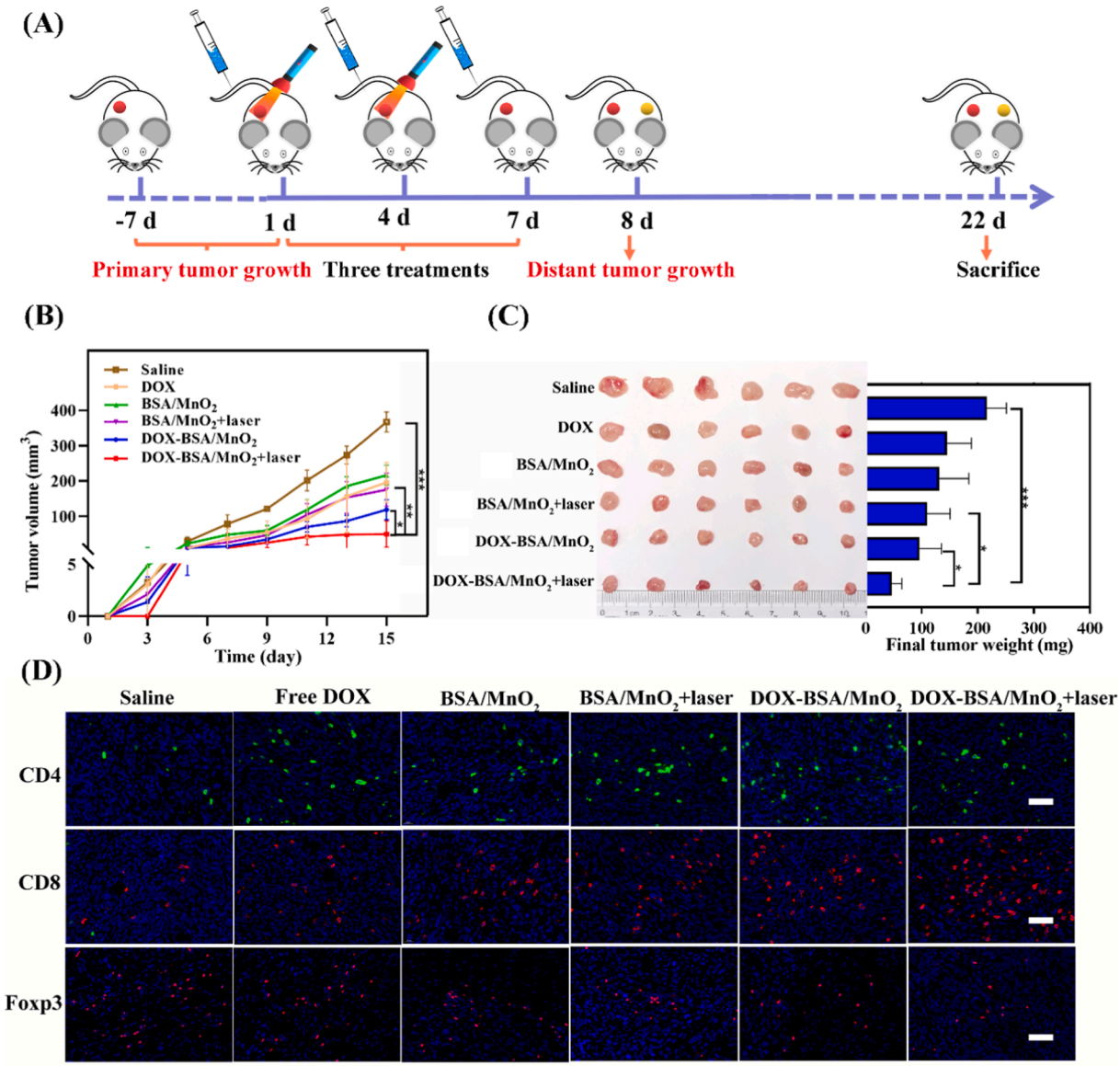

Fig. 7. Distant tumor inhibition assay. (A) Schematic illustration of the experimental design with 4T1-bearing BALB/c mice. (B) Distant tumor growth curves of the 4T1-bearing BALB/c mouse model, n = 6. (C) Images and weights of distant tumors obtained from 4T1-bearing BALB/c mice, n = 6. (D) Representative immunofluorescence images of distant tumor tissues obtained from the different treatment groups and stained with DAPI (blue), CD4+ (green), CD8+ (red) and Foxp3+ (red) (scale bar = 100 μm). (For interpretation of the references to color in this figure legend, the reader is referred to the web version of this article.)

of the distant tumors after treatment of the primary tumors was recorded and plotted. The growth of the distant tumors showed varying degrees of retardation in the mice treated with formulations containing MnO_2, which confirmed that MnO_2 played an essential role in distant tumor inhibition and in the establishment of systemic immunity. The mice treated with the DOX, BSA/MnO_2 NPs, BSA/MnO_2 NPs plus laser irradiation and DOX-BSA/MnO_2 NPs showed moderate distant tumor inhibition. In comparison, in the DOX-BSA/MnO_2 NP plus laser irradiation group, the distant tumor was not visible until the third day, and the tumor volume on the last day was significantly smaller than that of the other groups. These results demonstrated that chemo-photothermal therapy with modulation of the TME could induce a stronger immune response than the individual treatments. Strikingly, the DOX-BSA/MnO_2 NP group achieved much better efficacy in the inhibition of distant tumors than the clinically used drug DOX. The tumor volume measurements were consistent with the final distant tumor weights (Fig. 7C). To better understand the improved tumor inhibition effect obtained with the DOX-BSA/MnO_2 NPs plus laser irradiation on distant tumors, the intratumor infiltration of CD8+ T cells, CD4+ T cells and Tregs was examined by immunofluorescence analysis. As illustrated in Fig. 7D, the tumor treated with the DOX-BSA/MnO_2 NPs plus laser irradiation contained more CD4+ and CD8+ T cells than the tumors of the other groups. In conclusion, the combination treatment of chemo-photothermal therapy and modulation of the TME provided by the DOX-BSA/MnO_2 NPs plus laser irradiation not only effectively slowed the growth of primary tumors but also inhibited the growth of distant tumors via the abscopal immune response.

4. Conclusion

In summary, we developed BSA-templated MnO_2 nanoparticles loaded with DOX (DOX-BSA/MnO_2 NPs) as a multifunctional therapeutic platform. Compared with previously reported MnO_2 nanostructures for tumor immunotherapy, the BSA-templated MnO_2 NPs developed in this study showed advantages in highly efficient photothermal conversion, highly effective drug loading and precisely

controlled drug release in the acidic TME. The relief of tumor hypoxia by the MnO_2-triggered decomposition of endogenous H_2O_2 inside tumors offered remarkable benefits for reversing the immunosuppressive TME to favor antitumor immunity after the first round of combined treatment (chemo-photothermal therapy). Furthermore, DOX-BSA/MnO_2 NP-mediated chemo-photothermal therapy effectively modified the immunosuppressive microenvironment to favor antitumor immunity, which exerted an abscopal effect to inhibit the growth of distant tumors through regulation of the immune cell composition. Due to its inherent biodegradability, our photothermal BSA-templated MnO2 nanoplatform may have significant potential for clinical translation to allow the combination of chemo-photothermal therapy with ICD-based immunotherapy. These therapies act together with modulation of the TME and could achieve a synergistic comprehensive effect in battling tumors. Considering the complexity of the immunosuppressive TME, our next step is to combine the BSA/MnO_2 NPs with immune checkpoint inhibitors (PD-L1/PD-1) to achieve better antitumor effects.

CRediT authorship contribution statement

Zhenzhen Chen: Conceptualization, Methodology, Formal analysis, Writing – original draft, Visualization, Investigation. **Qian Zhang:** Conceptualization, Methodology, Investigation, Funding acquisition. **Qinbiao Huang:** Methodology, Resources. **Zhihong Liu:** Conceptualization, Resources. **Lingjun Zeng:** Conceptualization, Methodology, Investigation. **Lingna Zhang:** Resources, Visualization, Validation. **Xu Chen:** Formal analysis, Validation. **Hongtao Song:** Conceptualization, Methodology, Supervision, Project administration, Writing – review & editing, Funding acquisition, Visualization. **Jialiang Zhang:** Conceptualization, Methodology, Supervision, Writing – review & editing, Visualization.

Declaration of Competing Interest

The authors declare that they have no known competing financial interests or personal relationships that could have appeared to influence the work reported in this paper.

Acknowledgments

We gratefully thank Tao Chun (Jiaxing Customs, PRC) for the experiment guidance. We would like to thank Junjin Lin, Shuping Zheng, Zhihong Huang from the Public Technology Service Center (Fujian Medical University, Fuzhou, China) for their technical assistance.

Funding sources

We gratefully acknowledge the financial support of the Natural ScienceFoundation of Fujian Province (Grant no. 2021J01690).

Appendix A. Supplementary material

Supplementary data to this article can be found online at https://doi.org/10.1016/j.ijpharm.2022.121578.

References

Ahmad, A., Khan, F., Mishra, R.K., Khan, R., 2019. Precision Cancer Nanotherapy: Evolving Role of Multifunctional Nanoparticles for Cancer Active Targeting. J. Med. Chem. 62 (23), 10475–10496. https://doi.org/10.1021/acs.jmedchem.9b00511.

Alibolandi, M., Sadeghi, F., Abnous, K., Atyabi, F., Ramezani, M., Hadizadeh, F., 2015. The chemotherapeutic potential of doxorubicin-loaded PEG-b-PLGA nanopolymersomes in mouse breast cancer model. Eur. J. Pharm. Biopharm. 94, 521–531. https://doi.org/10.1016/j.ejpb.2015.07.005.

Bezu, L., Gomes-da-Silva, L.C., Dewitte, H., Breckpot, K., Fucikova, J., Spisek, R., Galluzzi, L., Kepp, O., Kroemer, G., 2015. Combinatorial strategies for the induction of immunogenic cell death. Front. Immunol. 6, 187. https://doi.org/10.3389/fimmu.2015.00187.

Chao, Y., Liang, C., Tao, H., Du, Y., Wu, D., Dong, Z., Jin, Q., Chen, G., Xu, J., Xiao, Z., Chen, Q., Wang, C., Chen, J., Liu, Z., 2020. Localized cocktail chemoimmunotherapy after in situ gelation to trigger robust systemic antitumor immune responses. Sci. Adv. 6, eaaz4204. https://doi.org/10.1126/sciadv.aaz4204.

Chen, Q., Liang, C., Wang, C., Liu, Z., 2015. An imagable and photothermal "Abraxane-Like" nanodrug for combination cancer therapy to treat subcutaneous and metastatic breast tumors. Adv. Mater. 27 (5), 903–910. https://doi.org/10.1002/adma.201404308.

Chen, Q., Feng, L., Liu, J., Zhu, W., Dong, Z., Wu, Y., Liu, Z., 2016. Intelligent Albumin-MnO2 Nanoparticles as pH-/H2 O2 -Responsive Dissociable Nanocarriers to Modulate Tumor Hypoxia for Effective Combination Therapy. Adv. Mater. 28 (33), 7129–7136. https://doi.org/10.1002/adma.201601902.

Ding, B., Zheng, P., Jiang, F., Zhao, Y., Wang, M., Chang, M., Ma, P.A., Lin, J., 2020. MnO nanospikes as nanoadjuvants and immunogenic cell death drugs with enhanced antitumor immunity and antimetastatic effect. Angew. Chem. Int. Ed. Engl. 59, 16381–16384. https://doi.org/10.1002/anie.202005111.

Ding, B., Yue, J., Zheng, P., Ma, P., Lin, J., 2021. Manganese oxide nanomaterials boost cancer immunotherapy. J. Mater. Chem. B 9 (35), 7117–7131. https://doi.org/10.1039/d1tb01001h.

Duan, X., Chan, C., Lin, W., 2019. Nanoparticle-mediated immunogenic cell death enables and potentiates cancer immunotherapy. Angew. Chem. Int. Ed. 58 (3), 670–680. https://doi.org/10.1002/anie.201804882.

Elsadek, B., Kratz, F., 2012. Impact of albumin on drug delivery—New applications on the horizon. J. Control. Release 157 (1), 4–28. https://doi.org/10.1016/j.jconrel.2011.09.069.

Fan, H., Yan, G., Zhao, Z., Hu, X., Zhang, W., Liu, H., Fu, X., Fu, T., Zhang, X.B., Tan, W., 2016. A Smart photosensitizer–manganese dioxide nanosystem for enhanced photodynamic therapy by reducing glutathione levels in cancer cells. Angew. Chem. Int. Ed. 55 (18), 5477–5482. https://doi.org/10.1002/anie.201510748.

Feng, B., Niu, Z., Hou, B.o., Zhou, L., Li, Y., Yu, H., 2020. Enhancing triple negative breast cancer immunotherapy by ICG-templated self-assembly of paclitaxel nanoparticles. Adv. Funct. Mater. 30 (6), 1906605. https://doi.org/10.1002/adfm.201906605.

Galluzzi, L., Vitale, I., Warren, S., Adjemian, S., Agostinis, P., Martinez, A.B., Chan, T.A., Coukos, G., Demaria, S., Deutsch, E., Draganov, D., Edelson, R.L., Formenti, S.C., Fucikova, J., Gabriele, L., Gaipl, U.S., Gameiro, S.R., Garg, A.D., Golden, E., Han, J., Harrington, K.J., Hemminki, A., Hodge, J.W., Hossain, D.M.S., Illidge, T., Karin, M., Kaufman, H.L., Kepp, O., Kroemer, G., Lasarte, J.J., Loi, S., Lotze, M.T., Manic, G., Merghoub, T., Melcher, A.A., Mossman, K.L., Prosper, F., Rekdal, Ø., Rescigno, M., Riganti, C., Sistigu, A., Smyth, M.J., Spisek, R., Stagg, J., Strauss, B.E., Tang, D., Tatsuno, K., van Gool, S.W., Vandenabeele, P., Yamazaki, T., Zamarin, D., Zitvogel, L., Cesano, A., Marincola, F.M., 2020. Consensus guidelines for the definition, detection and interpretation of immunogenic cell death. J. Immunother. Cancer. 8 (1), e000337. https://doi.org/10.1136/jitc-2019-000337.

Galon, J., Bruni, D., 2019. Approaches to treat immune hot, altered and cold tumours with combination immunotherapies. Nat. Rev. Drug. Discov. 18 (3), 197–218. https://doi.org/10.1038/s41573-018-0007-y.

Gao, F., Tang, Y., Liu, W.L., Zou, M.Z., Huang, C., Liu, C.J., Zhang, X.Z., 2019. Intra/extracellular lactic acid exhaustion for synergistic metabolic therapy and immunotherapy of tumors. Adv. Mater. 31 (51), 1904639. https://doi.org/10.1002/adma.201904639.

Gindy, M.E., Prud'homme, R.K., 2009. Multifunctional nanoparticles for imaging, delivery and targeting in cancer therapy. Expert Opin. Drug Del. 6 (8), 865–878. https://doi.org/10.1517/17425240902932908.

Habash, R.W.Y., Bansal, R., Krewski, D., Alhafid, H.T., 2006. Thermal Therapy, Part 1: An Introduction to Thermal Therapy. Crit. Rev. Biomed. Eng. 34 (6), 459–489. https://doi.org/10.1615/CritRevBiomedEng.v34.i6.20.

Hafez, A.A., Naserzadeh, P., Ashtari, K., Mortazavian, A.M., Salimi, A., 2018. Protection of manganese oxide nanoparticles-induced liver and kidney damage by vitamin D. Regul. Toxicol. Pharm. 98, 240–244. https://doi.org/10.1016/j.yrtph.2018.08.005.

He, Q., Zhang, Z., Liu, H., Tuo, Z., Zhou, J., Hu, Y., Sun, Y., Wan, C., Xu, Z., Lovell, J.F., Hu, D., Yang, K., Jin, H., 2020. Relieving immunosuppression during long-term anti-angiogenesis therapy using photodynamic therapy and oxygen delivery. Nanoscale 12, 14788–14800. https://doi.org/10.1039/d0nr02750b.

Heshmati Aghda, N., Abdulsahib, S.M., Severson, C., Lara, E.J., Torres Hurtado, S., Yildiz, T., Castillo, J.A., Tunnell, J.W., Betancourt, T., 2020. Induction of immunogenic cell death of cancer cells through nanoparticle-mediated dual chemotherapy and photothermal therapy. Int. J. Pharm. 589, 119787. https://doi.org/10.1016/j.ijpharm.2020.119787.

Hou, L., Tian, C., Yan, Y., Zhang, L., Zhang, H., Zhang, Z., 2020. Manganese-based nanoactivator optimizes cancer immunotherapy via enhancing innate immunity. ACS Nano 14 (4), 3927–3940. https://doi.org/10.1021/acsnano.9b06111.

Janicka, M., Gubernator, J., 2017. Use of nanotechnology for improved pharmacokinetics and activity of immunogenic cell death inducers used in cancer chemotherapy. Expert. Opin. Drug. Del. 14 (9), 1059–1075. https://doi.org/10.1080/17425247.2017.1266333.

Kabingu, E., Oseroff, A.R., Wilding, G.E., Gollnick, S.O., 2009. Enhanced systemic immune reactivity to a basal cell carcinoma associated antigen following photodynamic therapy. Clin. Cancer. Res. 15 (13), 4460–4466. https://doi.org/10.1158/1078-0432.CCR-09-0400.

Kroemer, G., Galluzzi, L., Kepp, O., Zitvogel, L., 2013. Immunogenic cell death in cancer therapy. Annu. Rev. Immunol. 31 (1), 51–72. https://doi.org/10.1146/annurev-immunol-032712-100008.

Laoui, D., Van Overmeire, E., Di Conza, G., Aldeni, C., Keirsse, J., Morias, Y., Movahedi, K., Houbracken, I., Schouppe, E., Elkrim, Y., Karroum, O., Jordan, B., Carmeliet, P., Gysemans, C., De Baetselier, P., Mazzone, M., Van Ginderachter, J.A., 2014. Tumor hypoxia does not drive differentiation of tumor-associated macrophages but rather fine-tunes the M2-like macrophage population. Cancer Res. 74, 24. https://doi.org/10.1158/0008-5472.

Li, W., Yang, J., Luo, L., Jiang, M., Qin, B., Yin, H., Zhu, C., Yuan, X., Zhang, J., Luo, Z., Du, Y., Li, Q., Lou, Y., Qiu, Y., You, J., 2019. Targeting photodynamic and photothermal therapy to the endoplasmic reticulum enhances immunogenic cancer cell death. Nat. Commun. 10, 3349. https://doi.org/10.1038/s41467-019-11269-8.

Li, J., Yu, X., Jiang, Y., He, S., Zhang, Y., Luo, Y.u., Pu, K., 2021. Second near-infrared photothermal semiconducting polymer nanoadjuvant for enhanced cancer immunotherapy. Adv. Mater. 33 (4), 2003458. https://doi.org/10.1002/adma.202003458.

Liang, R., Wei, M., Evans, D.G., Duan, X., 2014. Inorganic nanomaterials for bioimaging, targeted drug delivery and therapeutics. Chem. Commun. 50 (91), 14071–14081. https://doi.org/10.1039/C4CC03118K.

Liu, Z., Zhang, S., Lin, H., Zhao, M., Yao, H., Zhang, L., Peng, W., Chen, Y., 2018. Theranostic 2D ultrathin MnO2 nanosheets with fast responsibility to endogenous tumor microenvironment and exogenous NIR irradiation. Biomaterials 155, 54–63. https://doi.org/10.1016/j.biomaterials.2017.11.015.

Lv, W., Cao, M., Liu, J., Hei, Y., Bai, J., 2021. Tumor microenvironment-responsive nanozymes achieve photothermal-enhanced multiple catalysis against tumor hypoxia. Acta Biomater. 135, 617–627. https://doi.org/10.1016/j.actbio.2021.08.015.

Maksimenko, O., Malinovskaya, J., Shipulo, E., Osipova, N., Razzhivina, V., Arantseva, D., Yarovaya, O., Mostovaya, U., Khalansky, A., Fedoseeva, V., Alekseeva, A., Vanchugova, L., Gorshkova, M., Kovalenko, E., Balabanyan, V., Melnikov, P., Baklaushev, V., Chekhonin, V., Kreuter, J., Gelperina, S., 2019. Doxorubicin-loaded PLGA nanoparticles for the chemotherapy of glioblastoma: Towards the pharmaceutical development. Int. J. Pharm. 572, 118733 https://doi.org/10.1016/j.ijpharm.2019.118733.

Pan, J., Wang, Y., Pan, H., Zhang, C., Zhang, X., Fu, Y.Y., Zhang, X., Yu, C., Sun, S.K., Yan, X.P., 2017. Mimicking drug–substrate interaction: a smart bioinspired technology for the fabrication of theranostic nanoprobes. Adv. Funct. Mater. 27 (3), 1603440. https://doi.org/10.1002/adfm.201603440.

Pan, J., Wang, Y., Zhang, C., Wang, X., Wang, H., Wang, J., Yuan, Y., Wang, X., Zhang, X., Yu, C., Sun, S.K., Yan, X.P., 2018. Antigen-directed fabrication of a multifunctional nanovaccine with ultrahigh antigen loading efficiency for tumor photothermal-immunotherapy. Adv. Mater. 30 (8), 1704408. https://doi.org/10.1002/adma.201704408.

Petros, R.A., DeSimone, J.M., 2010. Strategies in the design of nanoparticles for therapeutic applications. Nat. Rev. Drug Discov. 9 (8), 615–627. https://doi.org/10.1038/nrd2591.

Pollard, J.W., 2004. Tumour-educated macrophages promote tumour progression and metastasis. Nat. Rev. Cancer 4 (1), 71–78. https://doi.org/10.1038/nrc1256.

Qian, X., Han, X., Yu, L., Xu, T., Chen, Y., 2020. Manganese-based functional nanoplatforms: nanosynthetic construction, physiochemical property, and theranostic applicability. Adv. Funct. Mater. 30 (3), 1907066. https://doi.org/10.1002/adfm.201907066.

Rahman, M., Ahmad, M.Z., Kazmi, I., Akhter, S., Afzal, M., Gupta, G., Jalees Ahmed, F., Anwar, F., 2012. Advancement in multifunctional nanoparticles for the effective treatment of cancer. Expert Opin. Drug Del. 9 (4), 367–381. https://doi.org/10.1517/17425247.2012.668522.

Sau, S., Alsaab, H.O., Bhise, K., Alzhrani, R., Nabil, G., Iyer, A.K., 2018. Multifunctional nanoparticles for cancer immunotherapy: A groundbreaking approach for reprogramming malfunctioned tumor environment. J. Controll. Release. 274, 24–34. https://doi.org/10.1016/j.jconrel.2018.01.028.

Singh, S.P., Kumari, M., Kumari, S.I., Rahman, M.F., Mahboob, M., Grover, P., 2013. Toxicity assessment of manganese oxide micro and nanoparticles in Wistar rats after 28 days of repeated oral exposure. J. Appl. Toxicol. 33 (10), 1165–1179. https://doi.org/10.1002/jat.2887.

Sun, D., Zhang, J., Wang, L., Yu, Z., O'Driscoll, C.M., Guo, J., 2021. Nanodelivery of immunogenic cell death-inducers for cancer immunotherapy. Drug Discov. Today 26 (3), 651–662. https://doi.org/10.1016/j.drudis.2020.11.029.

Takahashi, K., Kenji, A., Norihiro, T., Eisaku, K., Takashi, O., Kazuhiko, H., Tadashi, Y., Tadaatsu, A., 2001. Morphological interactions of interdigitating dendritic cells with B and T Cells in human mesenteric lymph nodes. Am. J. Pathol. 159 (1), 131–138. https://doi.org/10.1016/S0002-9440(10)61680-X.

Tang, Q., Cheng, Z., Yang, N., Li, Q., Wang, P., Chen, D., Wang, W., Song, X., Dong, X., 2019. Hydrangea-structured tumor microenvironment responsive degradable nanoplatform for hypoxic tumor multimodal imaging and therapy. Biomaterials 205, 1–10. https://doi.org/10.1016/j.biomaterials.2019.03.005.

Tang, H., Qiao, J., Fu, Y.X., 2016. Immunotherapy and tumor microenvironment. Cancer Lett. 370 (1), 85–90. https://doi.org/10.1016/j.canlet.2015.10.009.

Tian, L., Chen, Q., Yi, X., Chen, J., Liang, C., Chao, Y.u., Yang, K., Liu, Z., 2017. Albumin-Templated manganese dioxide nanoparticles for enhanced radioisotope therapy. Small 13 (25), 1700640. https://doi.org/10.1002/smll.201700640.

Vanneman, M., Dranoff, G., 2012. Combining immunotherapy and targeted therapies in cancer treatment. Nat. Rev. Cancer 12 (4), 237–251. https://doi.org/10.1038/nrc3237.

Wang, C., Bai, J., Liu, Y., Jia, X., Jiang, X., 2016. X. Jiang, Polydopamine coated selenide molybdenum: A new photothermal nanocarrier for highly effective chemo-photothermal synergistic therapy. ACS Biomater. Sci. Eng. 2 (11), 2011–2017. https://doi.org/10.1021/acsbiomaterials.6b00416.

Wang, Q., Zhang, Y., Wang, X., Wu, Y., Dong, C., Shuang, S., 2019. Dual role of BSA for synthesis of MnO nanoparticles and their mediated fluorescent turn-on probe for glutathione determination and cancer cell recognition. Analyst 144, 1988–1994. https://doi.org/10.1039/c8an02501k.

Xiao, B., Zhou, X., Xu, H., Wu, B., Hu, D., Hu, H., Pu, K., Zhou, Z., Liu, X., Tang, J., Shen, Y., 2018. Integration of polymerization and biomineralization as a strategy to facilely synthesize nanotheranostic agents. ACS Nano 12 (12), 12682–12691. https://doi.org/10.1021/acsnano.8b07584.

Xiao, B., Li, D., Xu, H., Zhou, X., Xu, X., Qian, Y., Yu, F., Hu, H., Zhou, Z., Liu, X., Gao, J., Slater, N.K.H., Shen, Y., Tang, J., 2021. An MRI-trackable therapeutic nanovaccine preventing cancer liver metastasis. Biomaterials 274, 120893. https://doi.org/10.1016/j.biomaterials.2021.120893.

Xu, X., Duan, J., Liu, Y., Kuang, Y., Duan, J., Liao, T., Xu, Z., Jiang, B., Li, C., 2021. Multi-stimuli responsive hollow MnO-based drug delivery system for magnetic resonance imaging and combined chemo-chemodynamic cancer therapy. Acta Biomater. 126, 445–462. https://doi.org/10.1016/j.actbio.2021.03.048.

Yang, G., Xu, L., Chao, Y., Xu, J., Sun, X., Wu, Y., Peng, R., Liu, Z., 2017. Hollow MnO2 as a tumor-microenvironment-responsive biodegradable nano-platform for combination therapy favoring antitumor immune responses. Nat. Commun. 8, 902. https://doi.org/10.1038/s41467-017-01050-0.

Yang, G., Ji, J., Liu, Z., 2021. Multifunctional MnO2 nanoparticles for tumor microenvironment modulation and cancer therapy. Wiley Interdiscip. Rev. Nanomed. Nanobiotechnol. 13 (6), e1720 https://doi.org/10.1002/wnan.1720.

Yu, M., Duan, X., Cai, Y., Zhang, F., Jiang, S., Han, S., Shen, J., Shuai, X., 2019. Multifunctional nanoregulator reshapes immune microenvironment and enhances immune memory for tumor immunotherapy. Adv. Sci. 6 (16), 1900037. https://doi.org/10.1002/advs.201900037.

Yuan, C., Deng, Z., Qin, D., Mu, Y., Chen, X., Liu, Y., 2021. Hypoxia-modulatory nanomaterials to relieve tumor hypoxic microenvironment and enhance immunotherapy: Where do we stand? Acta Biomater. 125, 1–28. https://doi.org/10.1016/j.actbio.2021.02.030.

Zhang, C.Y., Gao, J., Wang, Z., 2018. Bioresponsive Nanoparticles Targeted to Infectious Microenvironments for Sepsis Management. Adv. Mater. 30 (43), 1803618. https://doi.org/10.1002/adma.201803618.

Zhang, Z., Sang, W., Xie, L., Li, W., Li, B., Li, J., Tian, H., Yuan, Z., Zhao, Q.i., Dai, Y., 2021. Polyphenol-based nanomedicine evokes immune activation for combination cancer treatment. Angew. Chem. Int. Ed. 60 (4), 1967–1975. https://doi.org/10.1002/anie.202013406.

Zhang, M., Xing, L., Ke, H., He, Y., Cui, P., Zhu, Y., Jiang, G., Qiao, J.-B., Lu, N., Chen, H., Jiang, H., 2017. MnO-based nanoplatform serves as drug vehicle and MRI contrast agent for cancer theranostics. ACS Appl. Mater. Interfaces 9, 11337–11344. https://doi.org/10.1021/acsami.6b15247.

Zhao, P., Li, L., Zhou, S., Qiu, L., Qian, Z., Liu, X., Cao, X., Zhang, H., 2018. TPGS functionalized mesoporous silica nanoparticles for anticancer drug delivery to overcome multidrug resistance. Mater. Sci. Eng. C. 84, 108–117. https://doi.org/10.1016/j.msec.2017.11.040.

Zheng, P., Ding, B., Jiang, Z., Xu, W., Li, G., Ding, J., Chen, X., 2021. Ultrasound-augmented mitochondrial calcium ion overload by calcium nanomodulator to induce immunogenic cell death. Nano Lett. 21 (5), 2088–2093. https://doi.org/10.1021/acs.nanolett.0c04778.

Zhou, M., Wang, X., Lin, S., Cheng, Y., Zhao, S., Lin, J., Fang, Z., Lou, Z., Qin, L., Wei, H., 2020. Multifunctional STING-Activating Mn3O4@Au-dsDNA/DOX Nanoparticle for Antitumor Immunotherapy. Adv. Healthc. Mater. 9 (13), 2000064. https://doi.org/10.1002/adhm.202000064.

Zhou, F., Wang, M., Luo, T., Qu, J., Chen, W.R., 2021. Photo-activated chemo-immunotherapy for metastatic cancer using a synergistic graphene nanosystem. Biomaterials 265, 120421. https://doi.org/10.1016/j.biomaterials.2020.120421.

Zhou, M., Wang, X., Lin, S., Liu, Y., Lin, J., Jiang, B.o., Zhao, X., Wei, H., 2021. Combining Photothermal Therapy-Induced Immunogenic Cell Death and Hypoxia Relief-Benefited M1-Phenotype Macrophage Polarization for Cancer Immunotherapy. Adv. Ther. 4 (2), 2000191. https://doi.org/10.1002/adtp.202000191.

Zhu, Y., Xue, J., Chen, W., Bai, S., Zheng, T., He, C., Guo, Z., Jiang, M., Du, G., Sun, X., 2020. Albumin-biomineralized nanoparticles to synergize phototherapy and immunotherapy against melanoma. J. Controll. Release 322, 300–311. https://doi.org/10.1016/j.jconrel.2020.03.045.

Zhuang, H., Zhao, M., Ding, S., Liu, L., Yuan, W., Jiang, L., Han, X., Jiang, L., Yi, T., 2020. Multifunctional smart yolk–shell nanostructure with mesoporous MnO_2 shell for enhanced cancer therapy. ACS Appl. Mater. 12, 38906–38917. https://doi.org/10.1021/acsami.0c08389.